

**Enhanced photoelectrochemical water splitting performance by
CoFe₂S₄/TiO₂ nanotubes p-n type heterojunction**



Noor Alam

Reg.No. (00000278344)

A thesis submitted in partial fulfilment of the requirements for the degree of

Master in Science (MS)

In

Chemistry

Supervised by: Dr. Asad Mumtaz

Department of Chemistry


School of Natural Sciences

National University of Science and Technology H-12,


Islamabad, Pakistan December 2021

National University of Sciences & Technology**MS THESIS WORK**

We hereby recommend that the dissertation prepared under our supervision by: NOOR ALAM, Regn No. 00000278344 Titled: Enhanced photoelectrochemical water splitting performance by CoFe₂S₄/TiO₂ nanotubes p-n type heterojunction Be Accepted in partial fulfillment of the requirements for the award of **MS** degree.

Examination Committee Members1. Name: PROF. MANZAR SOHAILSignature: 2. Name: DR. M. ADIL MANSOORSignature: External Examiner: DR. SAIRA ARIFSignature: Supervisor's Name DR. ASAD MUMTAZSignature: 

 Head of Department

13/01/22
 Date
COUNTERSIGNED

 Date: 13/01/2022

 Dean/Principal

DEDICATION

I affectionately dedicate this effort to each and every member of my honorable family especially to my parents, not forgetting my respected teachers and friends, who had a remarkable effort in this achievement.

“Basic Research is what I am doing when I don’t know what I am doing”

WERNHER VON BRAUN

Acknowledgement

BISMILLAHIRRAHMANIRRAHIM

Alhamdulillah, Praise be to Allah Almighty for his help and guidance that finally made me able to complete this thesis. First and foremost I offer my sincerest gratitude to my supervisor **Dr. Asad Mumtaz**, Assistant Professor, who has advised and guided me throughout my research with his patience and deepest knowledge.

❖ I would like to give my special thanks to my friends for sharing the ups and down throughout the completion of my research work and thesis. I pay my special regards and a lot of thanks to my **classmates** for encouragement and support especially at times when things were going tough.

❖ I cannot end without saying thanks to my family members, especially to my parents who support me financially and encourage me during my research work.

I hope, these studies will benefits to all of us.

Noor Alam

Abstract:

Earth-abundant photoelectrocatalyst with better photocatalytic activity and maximum stability are in greater demand for realizing systematic sustainable and efficient photocatalytic water splitting. Chalcogenides with suitable atomic arrangement and having high electronic transport, show unique interesting catalytic properties in overall photoelectrochemical water splitting. Here, a fabrication of multi-elements composition were proposed to develop $\text{CoFe}_2\text{S}_4/\text{TiO}_2$ nanotubes (NTs) heterojunction using anodization, followed by SILAR method and then its sulfurization via CVD technique. The synthesized photocatalyst were characterized using an X-ray diffraction (XRD), Raman spectroscopy, scanning electron microscopy (SEM), Energy-dispersive X-ray spectroscopy (EDS), UV-Vis-Diffuse reflectance spectroscopy (UV-Vis-DRS), Fourier transform infrared spectroscopy (FTIR) and Photoluminescence (PL) spectroscopy. Photoelectrochemical results determines that 15- $\text{CoFe}_2\text{S}_4/\text{TiO}_2$ NTs have excellent photocurrent density of 2.95 mAcm^{-2} , as compared to pure TiO_2 NTs (0.78 mAcm^{-2}), 05- $\text{CoFe}_2\text{S}_4/\text{TiO}_2$ NTs (1.04 mAcm^{-2}), 10- $\text{CoFe}_2\text{S}_4/\text{TiO}_2$ NTs (1.75 mAcm^{-2}), and 20- $\text{CoFe}_2\text{S}_4/\text{TiO}_2$ NTs (2.30 mAcm^{-2}) respectively at 0.3V vs Ag/AgCl (1.23V vs RHE) using 100 mWcm^{-2} light intensity without UV-Vis light filter. The better photocatalytic performance of 15- $\text{CoFe}_2\text{S}_4/\text{TiO}_2$ NTs is because of the optimized loading of CoFe_2S_4 over TiO_2 NTs having proper atomic arrangement and morphology, which is thus helpful in efficient charge separation and transportation with unique redox capability.

Keywords: photoelectrochemical water splitting, CoFe_2S_4 , TiO_2 nanotubes, p-n type photocatalyst

Table of Content

Contents

Abstract:.....	1
Table of Content	iii
List of Abbreviation.....	v
List of Figures	vi
List of Tables	vi
Chapter-01	1
Introduction:	1
1. Nanotubes:	1
1.1 Inorganic Nanotubes:	1
1.1.1 Physical properties of Inorganic Nanotubes:	1
1.1.2 Applications of Inorganic Nanotubes:.....	2
1.2 Titanium (Ti) :	3
1.3 Titanium (Ti) properties:	3
1.3.1 Physical Properties:.....	3
1.3.2 Chemical Properties:.....	3
1.4 Titanium Dioxide Nanotubes:	4
1.4.1 Occurance:	4
1.4.2 History of TiO ₂ :.....	4
1.4.3 Photocatalyst:	5
1.4.4 Hydroxyl radical formation:	5
1.5 Properties of TiO₂ :	6
1.5.1 Physical properties of TiO ₂ :.....	6
1.6 Various crystalline form of TiO₂ Nanotubes:	6
1.6.1 Anatase:	7
1.6.2 Rutile:.....	7
1.6.3 Brookite:.....	8
1.7 Applications of TiO₂ Nanotubes:	8
1.8 Methods of Synthesis of TiO₂ nanotubes:	9
1.8.1 Sol-Gel Transcription Synthesis:	9

1.8.2	Hydrothermal Synthesis:.....	9
1.8.3	Electrochemical Anodization Synthesis:	10
1.9	Water Splitting:	11
1.9.1	Photoelectrochemical water splitting:.....	12
1.9.2	Fundamental Concept:.....	15
1.10	Aims & Objectives:	21
Chapter_02		23
2.	Literature Review:	23
Chapter-03		41
3.	Materials & Methods:	41
3.1	Materials:.....	41
3.2	Apparatus:.....	41
3.3	Instruments & Equipments:	41
3.4	TiO ₂ nanotubes synthesis.....	41
3.5	CoFe ₂ S ₄ /TiO ₂ nanotubes synthesis:	42
3.6	Characterization:	44
3.6.1	Introduction to characterization techniques:	44
3.7	Photoelectrochemical measurement:.....	45
Chapter-04		48
4.	Results & Discussions:	48
4.1	XRD ANALYSIS:	48
4.2	SEM analysis along with Energy dispersive spectroscopy (EDS):.....	49
4.3	Raman Spectroscopy:.....	51
4.4	UV-Vis Diffuse Reflectance Spectroscopy:	52
4.5	Fourier Transform Infrared Spectroscopy (FTIR):	53
4.6	Fluorescence Spectroscopy (FL):	54
4.7	Photoelectrochemical Analysis (PEC):.....	54
4.8	Conclusion:	60
References:		Error! Bookmark not defined.

List of Abbreviation

TiO₂ NTs	:	Titanium dioxide nanotubes
XRD	:	X-ray Diffraction
Uv-Vis-DRS	:	Ultra Violet-Visible-Diffuse Reflectance Spectroscopy
CVD	:	Chemical Vapor Deposition
FL	:	Fluorescence Spectra
EIS	:	Electrochemical Impedance Spectroscopy
DI	:	Deionized
FTIR	:	Fourier Transform Spectroscopy

List of Figures

Figure 1 (a) Proposed PEC system (b) Photovoltaic panel	13
Figure 2 (a) Water splitting reaction (b) Photoanode band diagram (c) A three electrode system.	14
Figure 3. Schematic representation of photoelectrochemical water splitting	16
Figure 4 Photo-electrochemical water splitting cell with TiO ₂ NTs as an n-type semiconductor	21
Figure 5 TEM images and Raman spectra of the as-prepared TiO ₂ nanotubes	24
Figure 6. Experimental setup for Ti anodization	25
Figure 7. FESEM images at 680 °C (a) Before & (b) After.....	26
Figure 8 SEM images of TiO ₂ nanotubes (a) wire (b) substrate	27
Figure 9 Photocatalytic activity mechanism in CNTs/Fe–Ni/TiO ₂	28
Figure 11. The voltage drop from zero to –1.7 V before anodization.....	29
Figure 12 A comparison between different chalcogenides metals for hydrogen evolution.....	31
Figure 13 FE-SEM images of (a) TONT film, (b) the S-doped (450 °C) (c) 500 °C and (d) 550 °C.....	33
Figure 14 (a) Absorption spectrum & (b) TEM image of FeS ₂ NCs.	34
Figure 15 Synthesis procedure of FeS ₂ /TiO ₂ NTs. (a) Ti foil, (b) first anodized TiO ₂ NTs, (c) nanoconcaves (d) second anodized TiO ₂ NTs and (e) FeS ₂ /TiO ₂ NTs.	35
Figure 16 Formation of core-shell nanoboxes arrays on Ni foam.....	38
Figure 18 Schematic diagram for SILAR cycle and CVD technique.	43
Figure 17 Schematic diagram for anodization process.	43
Figure 19 XRD patterns of (a) pristine TiO ₂ NTs (b) 05 (c) 10 (d) 15 and (e) 20-CoFe ₂ S ₄ /TiO ₂ NTs...	49
Figure 20 SEM images of (a) 05 (b) 10 (c) 15 (d) 20-CoFe ₂ S ₄ /TiO ₂ NTs.....	50
Figure 21 EDS spectrum of (a) 15 (b) 20-CoFe ₂ S ₄ /TiO ₂ NTs	51
Figure 22 Raman Spectra of (a) Pristine TiO ₂ NTs (b) 05 (c) 10 (d) 15 (e) 20-CoFe ₂ S ₄ /TiO ₂ NTs.....	52
Figure 23 (a) UV-Vis & (b) DRS spectra of CoFe ₂ S ₄ powder, pristine TiO ₂ NTs, 05, 10, 15, 20-CoFe ₂ S ₄ /TiO ₂ NTs	53
Figure 24 (a) FTIR spectra pristine TiO ₂ NTs, 15 and 20-CoFe ₂ S ₄ /TiO ₂ NTs (b) FL spectra of Pristine TiO ₂ NTs and CoFe ₂ S ₄ /TiO ₂ NTs (05, 10, 15 and 20 cycles)	54
Figure 25 (a) LSV (J-V) curves & (b) Chronoamperometry (I-t) curves of TiO ₂ NTs, 05, 10, 15, and 20-CoFe ₂ S ₄ /TiO ₂ NTs	57
Figure 26 (a) Mott-Schottky plots of the samples (b) Nyquist plot of the photoanode (c) Bode plot of samples under light (d) Proposed mechanism of photoelectrocatalysts.....	60

List of Tables

Table 1 Summary of some basic nanocomposite (Heterostructure).....	36
Table 2 Comparison with references.....	56
Table 3 Summary of photoelectrochemical data	58

Chapter-01

Introduction

Chapter-01

Introduction:

1. Nanotubes:

Nanotubes are the nanoscale (in nanometer) structure of any materials with structure similar to the carbon nanotubes (CNTs). They possess varying diameter and having different tube lengths depending upon the reaction condition. Here we have focused on a single material nanotube i.e Titanium dioxide nanotubes (TiO_2 NTs).

1.1 Inorganic Nanotubes:

Inorganic nanotubes are cylindrical molecules mostly made up of metal oxide or group III-Nitride morphologically as well as structurally same as those of carbon nanotubes. They also occurs naturally in some minerals deposits[1, 2]

Linus Pauling in early 1930, stated that curved layers may present in minerals[3], some minerals like white asbestos also known as chrysotile [4], and imogolite[5], possess tubular structure. The first artificial inorganic nanotube was discovered when Reshef Tenne *et al.* revealed the production of tungsten disulfide nanotubes in 1992 [6]. After that, nanotubes of many inorganic materials such as manganese oxides and vanadium oxides have been synthesized which are being investigated for applications such as for use as material for cathode formation in batteries and as redox catalyst.

2D layered solids such as tungsten (IV) sulphide (WS_2), molybdenum disulfide (MoS_2), and tin (IV) sulphide (SnS_2) are common inorganic nanotubes [7]. In the macroscopic level, WS_2 and SnS_2 /tin (II) sulphide (SnS) nanotubes have been produced [8, 9]. Inorganic nanotubes are generated using typical ceramics such as zirconium dioxide (ZrO_2) [10], titanium dioxide (TiO_2) and zinc oxide (ZnO) [11].

1.1.1 Physical properties of Inorganic Nanotubes:

i.They are simple to synthesize and have a high crystallinity [12].

- ii. Depending on the composition of the initial components, they have high homogeneity and dispersion, as well as predetermined electrical conductivity.
- iii. They possess a needle-like shape, excellent adhesion to a wide range of polymers, and great impact resistance [13].
- iv. They're used as filler in polymer composites to improve their thermal, electrical and mechanical characteristics.
- v. Because inorganic nanotubes are heavier than carbon nanotubes and stronger when compressed, they are employed in bulletproof jackets.

1.1.2 Applications of Inorganic Nanotubes:

- i. By the addition of 0.01 weight percent of inorganic nanotubes to cellulose fibres, the mechanical strength may be improved by an enormous margin.
- ii. WS₂ nanotubes increased adhesion, ductility, as well as strain energy release rate in epoxy resin.
- iii. Poly (methyl methacrylate) fiber mesh with increased stiffness and strength due to the inclusion of inorganic nanotubes might be used as impact absorption media [14].
- iv. In order to protect, direct them to desired location or to develop new characteristics in filler, another substance can be used within inorganic tubes as they are hollow from inside. This filler material should be restricted within nanoscale level diameter [15].
- v. The use of tungsten disulfide nanotubes in biodegradable polymeric nanomaterials for bone tissue fabrication applications, has been examined [16].
- vi. The addition of tungsten disulfide nanotubes at a concentration of 0.02% increased the compression and torsional characteristics of poly(propylene fumarate) nanocomposites much more as compared to carbon nanotubes.

1.2 Titanium (Ti) :

"Titanium" is a transition lustrous element with the atomic number "22" and the symbol "Ti." They have a silver appearance, little density, and great strength, and are highly corrosion resistant in sea water, chlorine and aqua regia.

William Gregor discovered titanium in 1791, and M.H Klaproth named. Anatase, Rutile, and Brookite are the three crystalline states in which they are found. It can be found in nearly all living organisms, as well as in water, soil and rocks [17]. Titanium dioxide (TiO₂) is the most common titanium compound and is used as a photocatalyst.

Titanium's two most valuable qualities are corrosion resistance and a high strength-to-density ratio. Titanium has a similar strength as steel, however it is less dense when it is unalloyed.

1.3 Titanium (Ti) properties:

1.3.1 Physical Properties:

- i. Their strength-to-weight ratio is high [18].
- ii. Titanium is a strong, low-density metal that is lustrous, ductile and metallic white in appearance [19].
- iii. They possess a high melting point which is around 1650 degrees Celsius.
- iv. They are paramagnetic, has lower electrical as well as thermal conductivity.
- v. On cooling below the temperature as 0.49K, they behave like a superconductor [20, 21].
- vi. Titanium is a weak conductor and is non-magnetic in nature.

1.3.2 Chemical Properties:

- i. Titanium metal and its alloy immediately oxidize when exposed to air. At 1200°C in air and 610°C in pure O₂, it rapidly reacts with oxygen to generate titanium dioxide (TiO₂).
- ii. At room temperature, they slowly react with water and air to generate a secondary oxide covering that protects the bulk metal from further oxidation.
- iii. They are somewhat stable to H₂SO₄, HCl, chloride solution and most organic acids.
- iv. Titanium is a thermodynamically reactive metal and melting is only feasible in vacuum or in an inert atmosphere.

v.It can reacts with halogens and absorb hydrogen, H₂.

1.4 Titanium Dioxide Nanotubes:

A natural abundant oxide of “Titanium” is **Titanium Dioxide, Titanium (iv) Oxide** or **Titania**, denoted chemically as TiO₂[17]. Titanium dioxide is a white inorganic substance that has been utilized in a wide range of products for over a century. It is reliant on it because of its non-toxic, non-reactive, and luminous features, which safely enhance the whiteness and brightness of a wide range of materials.

It is the brighter and whitest known pigment, having reflective properties and the ability to scatter and absorb UV rays.

1.4.1 Occurrence:

Titanium dioxide nanotubes occurs as a, rutile, anatase, and brookite”[18] The most common type of titanium dioxide is rutile, which includes roughly 98 percent TiO₂ in the ore. Anatase and brookite can be converted into rutile when heated above temperature in the range 600-800°C.

1.4.2 History of TiO₂:

Akira Fujishima in 1967 discovered the photocatalytic characteristics of TiO₂ and reported in 1972 [19, 20].

Honda-Fujishima effect was named after the process that occurred on the surface of "TiO₂". TiO₂ as a photocatalyst in the form of thin films & nanoparticles has the potential to be used in energy generation, as it split water into molecular hydrogen and oxygen respectively. The resultant hydrogen might be utilised as a fuel. Doping TiO₂ nanotubes with carbon, graphene, metals, and non-metals, for example, can increase their efficiency.

Fujishima and his colleagues found the super-hydrophilicity phenomena in TiO₂ coated glass exposed to sunshine in 1995. As a result, self-cleaning glass and anti-fogging coatings have been developed.

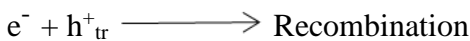
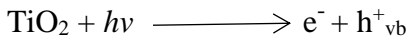
1.4.3 Photocatalyst:

When irradiated by UV rays, the nanosize TiO₂ nanotubes possess extraordinary photocatalytic activity in the anatase form. The planes of anatase show predominately more photocatalytic activity while in case of plane, the anatase are more thermodynamically stable as reported. The photocatalytic activity of biphasic titanium dioxide can be further boosted by allowing charge carrier separation at junctions of rutile and anatase. Finally, biphasic titanium dioxide is generally thought to have higher photocatalytic efficiency[26].

The positive holes' high oxidative potential oxidises water to form the hydroxyl radical, and they can also oxidise oxygen as well as other organic molecules effectively.

1.4.4 Hydroxyl radical formation:

Since anatase TiO₂ nanotubes absorb maximum UV light, which causes the hydroxyl radical to be generated ($\cdot\text{OH}$) [27]. At the top surface of TiO₂, when photo-generated holes in the valence bond (h^+_{vb}) are trapped, then trapped holes (h^+_{tr}) develop, which are incapable of oxidizing water.



$\lambda = 387 \text{ nm}$, The above reaction decomposes and degrades the undesirable compound present in the environment, especially in waste water[21] and in air. Thus anatase may be transformed into inorganic nanowire and nanotube.

1.5 Properties of TiO_2 :

1.5.1 Physical properties of TiO_2 :

A lot of distinctive physical features that is useful in a variety of applications:

- i) TiO_2 has a boiling point of $2,972^\circ\text{C}$ and a melting temperature of $1,843^\circ\text{C}$; hence it occurs in nature as a solid and in the form of particles. They are water insoluble.
- ii) TiO_2 is a dielectric.
- iii) It does not have yellowish look but are seems to be pure white.
- iv) Refractive index (Light scattering capacity) is greater compared to diamond, at 2.488 (anatase), 2.583 (brookite), and 2.609 (rutile).
- v) TiO_2 can exhibit photocatalytic capabilities when exposed to UV radiation.
- vi) They are low-cost, easily accessible, non-toxic, stable(chemically & mechanically), and possess a high turnover rate.
- vii) They are odorless, and white in color.
- viii) TiO_2 are non-toxic, have low synthesis cost, possess long-term chemical stability, highly ordered geometry, with best optical and electronic properties and one dimensional direction of electron movements.

1.6 Various crystalline form of TiO_2 Nanotubes:

The three main important crystalline form of TiO_2 nanotubes are;

1.6.1 Anatase:

In 1801, Rene Just Hauy termed the material "Anatase". The word is derived from the Greek word "anataxis," which means "extension," referring to the crystal's vertical axis being lengthier than in rutile. Octahedrite was the term given to the crystal before it was given the name anatase, which was given because of the crystal's common octahedral habit. Other names for this mineral come from the well-known French locale of Oisanite and Dauphinite.

Titanium dioxide in the form of anatase is a metastable mineral (TiO_2). In their natural state, they are a black solid, but in their purest form, they are colorless or white.

Anatase crystallizes in a tetragonal shape and is always found as a tiny, solitary, and sharply formed crystal. At all temperatures and pressures, anatase is metastable, with rutile being the equilibrium polymorph. Because of its lower surface energy, anatase is often the first titanium dioxide phase to develop in many processes, and it is converted into rutile at higher temperatures. Rutile is optically positive, while anatase is optically negative.

1.6.2 Rutile:

The "Rutile" was first described in 1803 by Abraham Gottlob Werner. Rutile gets its name from the Latin word "rutilus," having the meaning of "red." They exhibit a deep red colour when viewed through transmitted light, as shown in some specimens.

Rutile is the prevalent pure form of TiO_2 , with greatest visible light refractive indices of almost any existing crystal, as well as substantial dispersion and birefringence. Rutile is the most thermodynamically stable polymorph of TiO_2 , with a lower total free energy than anatase & brookite metastable phases.

Rutile is a tetragonal that grows in a prismatic or acicular pattern with a preference for orientation along the c axis, or [001] direction. Because the [110] side of rutile has the lowest surface free energy and hence is thermodynamically more stable, this growth habit is possible [29]. Rutile grows in nanorods, nanowires, and other nanostructures with a c-axis orientation.

1.6.3 Brookite:

Armand Levy, a French mineralogist, identified Brookite in 1825. Brookite is the orthorhombic form of TiO₂, that can be found in a variety of polymorphic forms. Brookite, like anatase and rutile, is uncommon and has a photocatalytic process [30]. Brookite will return to the rutile structure at temperatures above roughly 750°C. Brookite is often brown, but it can also be yellowish, reddish brown or even black. Brookite has a refractive index of around 2.5, which is higher than diamond's refractive index of 2.42. They aren't fluorescent or radioactive in any way.

Brookite has a specific gravity of 4.098, which is between that of anatase (3.9) and rutile (4.2).

1.7 Applications of TiO₂ Nanotubes:

- ✓ **Electric Appliances:** Refrigerator and fluorescent light
- ✓ **Air Purification:** Deodorizing and elimination of air pollutants
- ✓ **Printing :** Offset printing
- ✓ **Energy Conversion :** Solar battery
- ✓ **Road:** Tunnel lights and NO₂ elimination, Self-cleaning
- ✓ **Car :** Side Mirror
- ✓ **Water splitting :** Hydrogen production of Hydrogen gas
- ✓ **Water purification :** Disinfection
- ✓ **Interior Residence :** Curtain and Wall paper
- ✓ **Exterior Residence :** Glass/Tent and Painting/Tile
- ✓ **Agriculture :** Deodorization, residual pesticides removal and hydroponic culture
- ✓ **Medical :** Cancer and Catheter/Operating room[18, 22].

1.8 Methods of Synthesis of TiO₂ nanotubes:

Among various synthesis techniques of TiO₂ NTs, the electrochemical anodization process[23, 24] have a superior properties than the others one. Some basic process are as under used for the preparation of TiO₂ nanotubes;

1.8.1 Sol-Gel Transcription Synthesis:

It's a low-temperature and wet-chemical approach for synthesizing oxide. Here, the hydrolysis of precursors occur following polycondensation result in the formation of a solid network known as gel. Metal alkoxide and metal chlorides are the most common starting materials in sol-gel process. Polymer fiber, super molecular compound or porous alumina are used as a model in sol-gel process, having diameter normally larger than 50nm [25-27].

Sol-gel transcription technique were firstly presented by Kang et al. (2009) for the formation of high ordered TiO₂ nanotubes[28]. In this report, titanium isopropoxide, Ti (OC₃H₇), was employed as a starting precursor in ethanol. On an alumina template, TiO₂ nanotubes were produced. After that, the sample was then dried for 12 hrs at room temperature under normal conditions before being annealed at 500°C to convert it to a crystalline phase. After removing the alumina template, the isolated TiO₂ nanotubes were obtained. It is impossible to create a well-ordered and aligned nanotubular structure by using sol-gel technique, which are the main disadvantage of this method. They are time consuming process where solvent and organic by-products removal are difficult. Because of the high energy and chemical requirements, they are not economically viable. Moreover, the raw materials utilised in this research are costly, prompting several research organisations to look for a different technique to synthesize TiO₂ nanotubes.

1.8.2 Hydrothermal Synthesis:

Hydrothermal synthesis is a heterogeneous process that takes place at high pressure and temperature in the presence of an aqueous solvent or mineralizer. This approach is critical for producing large, impurity and single crystals free of dislocation[38-40]. The development of

crystal takes place in an autoclave, which is a steel pressure vessel that holds nutrient and water. In the growth chamber, a temperature gradient must be maintained. Seed developing rate is increased by increasing solvent concentration, crystallisation temperature, and temperature gradient[41-43]. The TiO₂ nanoparticle is treated in a basic solution of NaOH, in an autoclave at 150°C temperature from 15 hours to several days [44]. TiO₂ nanoparticles are transformed to nanotubes, when Na⁺ and OH⁻ ions combine with TiO₂, generating bonds between Ti, O, Na and Ti with OH. To lower the high energy, the particles will be shifted to plane form and then rolled into the tubular form[45, 46]. However, during the hydrothermal technique nanostructured tubes are unable to form, which are well aligned and ordered i.e the main drawbacks of hydrothermal techniques. Furthermore, the hydrothermal approach needed a long reaction time and the addition of extremely concentrated NaOH, which made it impossible to create TiO₂ nanotubes of uniform size.

1.8.3 Electrochemical Anodization Synthesis:

Anodization of Ti metal with an appropriate electrolyte solution and reaction conditions can produce well-ordered, homogenous & vertical array of TiO₂ nanotubes. Here The establishment of a barrier layer is followed by the formation of a well-defined nanoporous structure, which leads to the formation of TiO₂ nanotubes[33, 47-49]. TiO₂ nanotubes grown on Ti foil are amorphous after anodization which must be crystallised using a high-temperature annealing procedure [50-52].

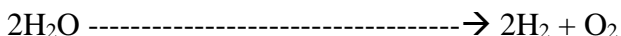
Electrochemical anodization is an electrolytic procedure that coats a metallic surface with a protective or ornamental oxide layer [53]. The electrochemical anodization approach for the TiO₂ nanotubes synthesis is chosen over the other ways because it is easier to prepare and handle and is more controlled. Vertically array of nanotubes, which feature tube-like structures with circular nanotubular openings that serve as a platform to anchor light-harvesting system, have a significant specific surface area[29, 30]. The nanotube diameter vary from 20 nm to 350 nm while it's length ranges from 0.2µm to 1000 µm depending on reaction conditions.

Domes is the lower portion of the nanotubes called barrier layer with typical hexagonal or pentagonal shape[31-33].

C. Ros et al. " Ti is used as an anode in an anodizing cell and is connected to the positive terminal of the power source, whereas platinum is utilised as the cathode and is connected to the negative terminal of the DC power supply[31, 34]. Carbon, lead, nickel, and stainless steel are some of the other materials utilised as cathodes. The cathode must be a nonreactive electrode in the electrolyte bath[35, 36]. The geometrical feature of nanotubes is mostly controlled by parameters such as anodization potential, electrolyte composition, and qualities such as conductivity and viscosity, as well as anodization time and temperature. Anodic oxide layer development, from a theoretical standpoint, entailed field assisted oxidation of anodic Ti film. The Ti–O bond polarisation will be induced by a strong electric field across the anodic oxide layer. The hollow (hole) will thereafter arise as a result of Ti–O polarisation. In the presence of fluoride ions, these random pits (cavities) will etch into nanotubular structure by chemical dissolution reaction." The table 01 above summarises the differences between the three techniques' distinct features.

Water Splitting:

The chemical reaction that breaks down water into oxygen and hydrogen is known as water splitting.



Water splitting occurs in photosynthesis but no hydrogen produced there, while hydrogen is produced due to water splitting in hydrogen fuel cell.

As people's knowledge on global warming has expanded, hydrogen fuel manufacturing has gotten a lot of attention. Hydrogen, a clean-burning fuel, is being produced using techniques like photocatalytic water splitting. The splitting of water has a lot of potential because it uses water, which is a cheap and renewable resource. The use of a catalyst and sunlight to create hydrogen from water is called photocatalytic water splitting.

1.8.4 Photoelectrochemical water splitting:

Energy saving procedure and renewable energy source should be applied worldwide, which are possible through advancement in technologies. As sun is one of the most abundant energy source, due to which owing to the universal abundance of water and pollution-free products, photoelectrochemical (PEC) water splitting is regarded one of the most efficient technologies, allowing hydrogen (H₂) to be used as a clean energy source. Fujishima and Honda (1970s) "TiO₂, an n-type semiconductor with a 3 eV band gap, in contact with an electrolyte, was able to absorb photons and generate enough potential to split the water molecule into hydrogen and oxygen, storing solar energy in chemical bonds, according to the PEC water splitting discovery."

A PEC device converts water into hydrogen and oxygen in the presence of a solar light source. PEC, on the other hand, was designed to operate at low current densities, in the tens of mAcm⁻² range, resulting in lower electrochemical overpotentials. Lower current densities enable the use of low-cost, abundant-on-earth catalysts. Furthermore, the PEC methodology is an easier architecture that reduces total investment expenses as well as electrical transmission inefficiencies [111].

Nevertheless, there are certain obstacles with PEC technology that must be overcome: corrosion must be prevented because the apparatus will be in close proximity to the electrolyte, and its configuration (design) will be restricted. Costs must be lower than hydrogen produced by fossil fuels for these technologies to be widely adopted, but environmental restrictions and levies could help in this direction. Although PEC systems offer a lot of potential, the costs of connected PV electrolyzers are unlikely to decline significantly in the near future.

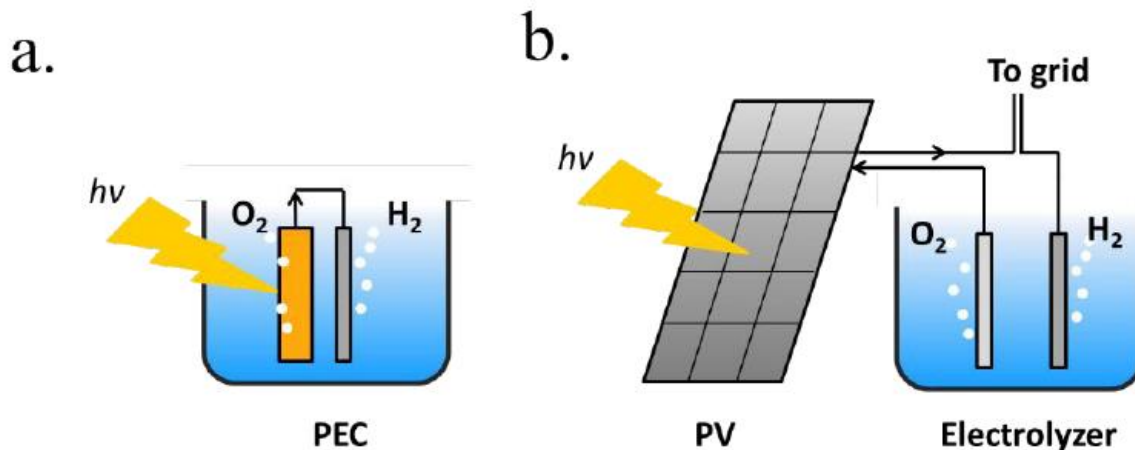


Figure 1 (a) Proposed PEC system (b) Photovoltaic panel

In PEC water splitting, photons are absorbed by the semiconductor, resulting in electron-hole pairs that are subsequently separated by the photo-built-in electrode's electric field. Ions physically adsorb to the surface of the semiconductor, generating a double layer with a diffuse outer layer and a quickly fading potential. The semiconductor's band bending then produces electric neutrality. As demonstrated in Figures (a) and (b), the built-in electric field can separate electron-hole pairs, resulting in photovoltage (V_{ph}) and photocurrent (b). In a photoanode, holes are carried to the photoelectrode's surface to carry out oxygen evolution, while electrons are caught by the back contact and the circuit is closed, allowing the counter electrode to perform the proton (H⁺) reduction reaction. A photocathode, on the other hand, is a semiconductor with a built-in electric field that forces electrons to the surface in order to carry out hydrogen evolution. It indicates that the photoanode produces oxygen (oxidation) or holes, whereas the photocathode produces hydrogen (reduction) or electrons. Photogenerated electron hole pairs will suffer over-potentials for charge separation (sep) and charge transport (trans) across the semiconductor, from the back contact and other elements in the circuit, for an outstanding photocurrent drive into the electrolyte to perform the water splitting reaction. According to some writers, the semiconductor material's minimum band gap ($E_{g \text{ min}}$) is >2.04 eV, based on:

$$E_{g \min} = \eta_{trans} + \eta_{sep} + V_{min} \dots\dots\dots(1)$$

If the photopotential of a single photoelectrode is insufficient, the reaction can be carried out with the help of an external bias. External power may be used in this scenario, but it can also help the photoelectrode produce more power.

In a "three electrodes" cell layout (or half-cell) (Figure c), each electrode can be monitored separately (at a fixed potential in respect to the electrolyte). In this system, an external power supply (or "potentiostat") supplies the required current to the counter electrode (CE), causing the desired potential to fall between the working electrode (WE) and a reference electrode (RE). The incoming light conversion efficiency into gas provided by this single electrode, known as half-cell solar-to-hydrogen (HCSTH) conversion efficiency, can be examined using this half-cell setup.

$$HC-STH (\%) = \frac{j_{ph} \times (E_{H_2O/O_2} - E)}{P_{sun}} \dots\dots\dots(2)$$

P_{sun} is the typical solar AM 1.5 irradiation, $100 \text{ mW} \cdot \text{cm}^{-2}$, and E_{H_2O/O_2} is the equilibrium redox potential of the oxygen evolution reaction (1.23 V vs RHE). The photocurrent density achieved is represented by j_{ph} , which is attained using an applied bias E . (relative to RHE).

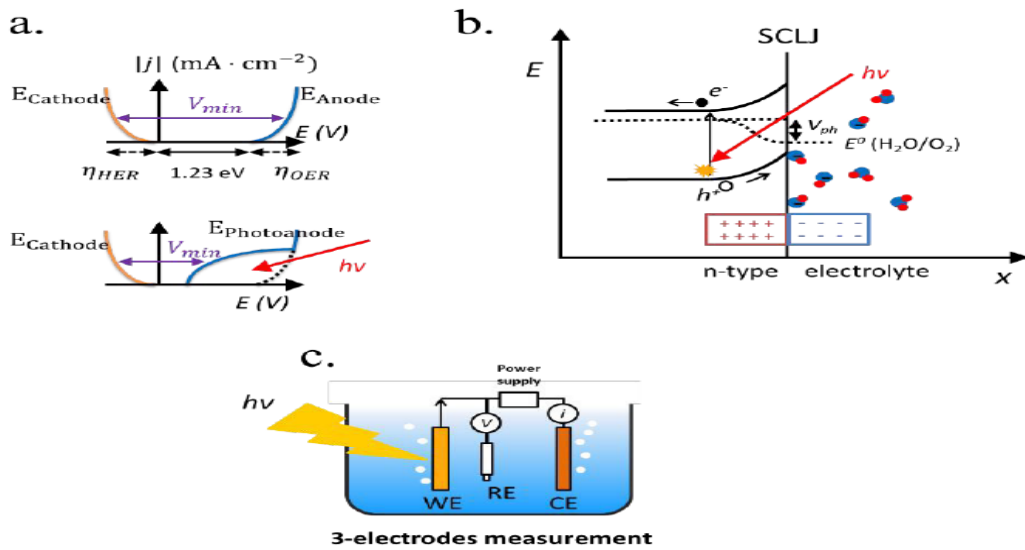


Figure 2 (a) Water splitting reaction (b) Photoanode band diagram (c) A three electrode system.

The following are the main requirements for productive PEC water splitting:

- ✓ Broad solar spectral absorption;
- ✓ Photogenerated electron-hole efficient excitation and separation property;
- ✓ Minimal transport losses between semiconductor and electrolyte working surface area;
- ✓ Very little overpotential when conducting the oxygen evolution reaction (OER) or hydrogen evolution reaction (HER);
- ✓ Stable for longer time
- ✓ Scalable device fabrication techniques
- ✓ Abundant materials having low cost

1.8.5 Fundamental Concept:

Photoelectrochemical water splitting is a complicated technique that involves a number of concepts and phenomena that should be tuned in order to develop an effective device. They are as follows:

- a) Interaction between light and matter
- b) Generation of electron & hole pairs
- c) Separation of charge and its transportation
- d) Charge transfer from catalyst surface to the electrolyte
- e) Reaction of splitting of water

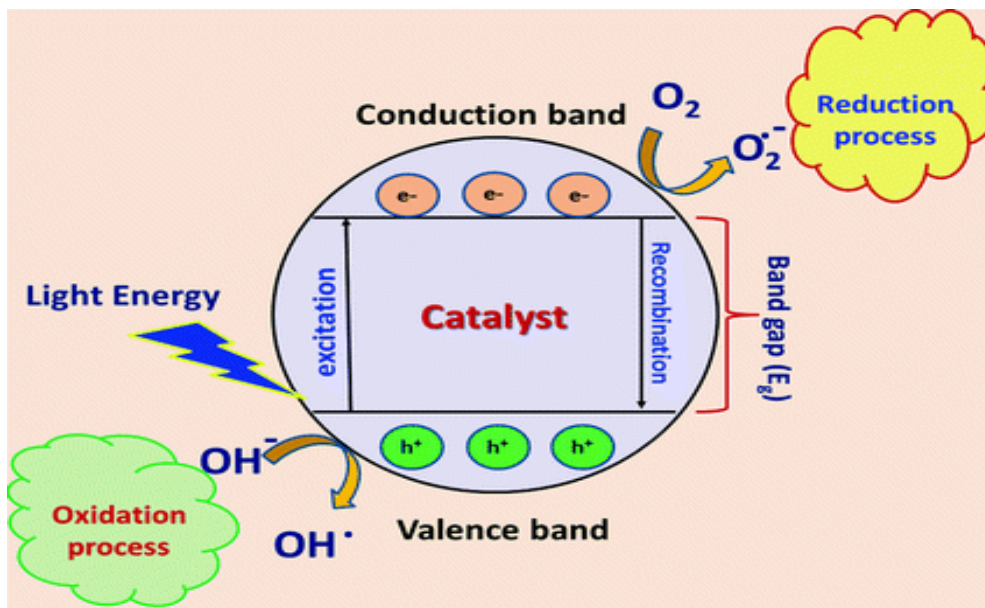


Figure 3. Schematic representation of photoelectrochemical water splitting

1.8.5.1 Light-matter interaction:

When a matter surface is strike by light, it may either reflected, refracted or transmitted. Light can be fractionally reflected or absorbed in some media, such as liquid electrolytes. To avoid large losses, a short transit distance through the electrolyte is required. Some incident light reflects at the interface between two media with dielectric constants that differ, propagating back into the original material. If the energy of photons is greater than the band gap of the substance, they can be absorbed inside it. Photon energy is delivered to atomic electrons in this situation, forming an electron-hole pair. An irradiation's penetration depth is a measurement of how deep it can enter a medium or material. It is a key characteristic in thin film semiconductors, ranging from 2 m for Si (at 555 nm wavelengths) to a few nanometers for iron oxide. Transmitted light is light that is not reflected or absorbed.

1.8.5.2 Electron-hole pair excitation:

When a substance absorbs a photon, the photon transfers its energy to an electron, which is subsequently stimulated to a higher energy level. In semiconductors, electrons can stay in

various states with varying average energies, generating valence and conduction bands. At absolute zero temperature, the valence band edge (E_v) is defined by the highest occupied molecular orbitals/states (HOMO), while the conduction band edge (E_c) is defined by the lowest unoccupied molecular orbitals (LUMO). The energy difference between these two states, where no states exist, is referred to as the forbidden energy region, or band gap (E_g).

Upon absorption, some of the valence band electrons (e^-) are stimulated into the conduction band, leaving an empty state known as a "hole" (h^+) in the network of covalent bonds. If a photon with more energy than the material's band gap is absorbed, the electron will consume the extra energy ("thermalize") until it reaches the conduction band edge. The excess energy from the excited electron is transferred to the neighbouring atoms in the form of thermal energy, and so the excited electron does not store all of the original photon's energy in the excited electron-hole pair form.

Some of these atoms are spontaneously ionised in semiconductors at a specific temperature, when electrons are excited to the conduction band and holes are produced in the valence band. The n- or p-type semiconductor behaviour is determined by the nature of the majority carriers produced, such as free electrons or vacancies, as well as defects in the covalent structure. By changing the number of acceptors or donors in a covalent structure, this n- or p-type semiconductor behaviour can be achieved. This phenomenon is called "*doping*" the semiconductor, and there are several forms to do it. The average states distribution energy is called the *Fermi level* (E_F). If Fermi level is closer to the valence band and maximum carriers are holes it is known as a **p-type** semiconductor, and if it is closer to conduction band and electrons are majority carriers, it is considered as **n-type** semiconductor.

1.8.5.3 Charge separation and transport:

To avoid recombination, electron-hole pairs must be goes away and separated when light strikes the materials. Due to the inability to obtained any current from photo-generated charges/carriers due to high recombination rates, efficient charge separation is required. To generate a photovoltage and a photocurrent, an external potential or an internal built-in potential is required to separate photogenerated charge carriers. When n- and p-type materials come into touch with

each other, a p-n junction is produced. Thus, charges spreading from one to the other, balance the average number of unbound electrons or holes in a system (Fermi levels), generating a space-charge or depletion zone with a strong electric field. Many structures, for example, have built-in electric fields:

- p-n heterojunction: Two materials with differing type characteristics come into contact with each other like (n-type TiO₂ & p-type silicon).

- p-n homojunction: Semiconductor with two separate type characters in each region (i.e. p-type and n-type silicon).

- A semiconductor-liquid junction (SCLJ): With the ions adsorbed on the surface, a Helmholtz double layer is produced, and the semiconductor is balanced (i.e. n-type TiO₂ in an alkaline electrolyte).

- Schottky junction: when the energy level of free electrons in a metallic layer is balanced by a semiconductor (Ni metal & n-type silicon).

An electric field then transfers the generated charges in opposite directions, with electrons flowing to the surface and holes going to the back contact. High conductivity is required for improved charge transmission. Carrier mobility and carrier concentration are both important factors in determining conductivity. Semiconductor impurities and defect density, on the other hand, have a significant impact on carrier mobility. These electrons and holes scatter extensively, losing energy and changing direction on crystallographic defects such as interstitial atoms or vacancies, plane dislocations, stacking faults, or grain boundaries. Furthermore, carrier concentration is affected by doping level, temperature, and illumination intensity. Charge transfer resistance will increase as a result of all of these causes.

1.8.5.4 Catalysis:

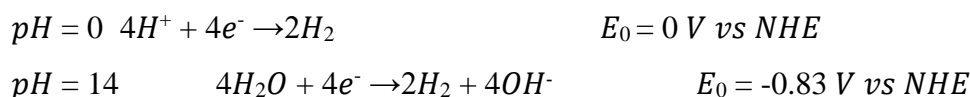
Once the electrons/holes reach the photo-surface, absorber's a chemical reaction happens (semiconductor). During the splitting of water, the hydrogen or oxygen evolution reaction occurs. As a result, not only is charge separation and electron/hole transport to the surface important, but so is the efficiency of the water splitting reaction and how electrons are moved to the reactants to obtain the products. Thus catalyst play an important role in accelerating a chemical reaction. An electro-catalyst is defined as a material repeatedly enhancing a certain

electrochemical reaction without being consumed. Catalysts introduce alternative reaction paths with lower activation energy through forming alternative intermediate species on its surface. As the reaction will happen on the surface, normally very small amounts of catalysts are needed.

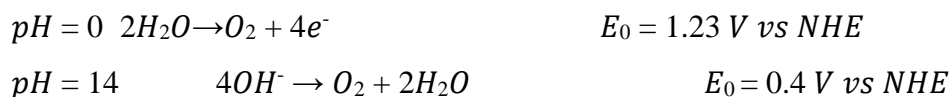
1.8.5.5 The water splitting reaction:

The reaction $2H_2O \rightarrow 2H_{2(g)} + O_{2(g)}$ is a non-spontaneous water splitting process. Water can be divided at room temperature by driving two half-reactions, the hydrogen evolution reaction (HER) and the oxygen evolution reaction (OER), by applying an electrical potential between a cathode and an anode immersed in an aqueous electrolyte (OER). The total Gibbs free energy of the reaction is 237.18 kJ/mol of generated H_2 , which corresponds to a thermodynamic reversible potential of 1.23 V. The potential values (E) are usually referenced in respect to the neutral hydrogen electrode (E vs NHE) or the reversible hydrogen electrode (E vs RHE), where the former is invariant with pH following $E_{RHE} = E_{NHE} + 0.059 \cdot pH$, and the potential values (E) are usually referenced in respect to the neutral hydrogen electrode (E vs NHE) or the reversible hydrogen electrode (E vs RHE). For example, at various pHs, the HER and OER standard potential values are:

HER:



OER:



Additionally, additional potentials for the catalysis, η_{HER} and η_{OER} , known as over-potentials, are required to proceed these reactions kinetically effective and systematic (with a high current

and therefore, productivity). For 10 mAcm⁻² currents and state-of-the-art catalysts, the over-potential for the water splitting process is 0.4 V. The type of electro-catalyst as well as the basic or acidic character of the electrolyte define the over-potential. For the process to go smoothly, the number of hydroxides (OH⁻) or protons (H⁺) present in the water dissociation kinetics is crucial. Furthermore, between the two electrodes, substantial ionic conductivity is required, which might result in an ohmic loss due to an extra potential (ionic cond.) at long distances or lower ion concentrations/conductivity. To avoid back-reactions if gases diffuse to the opposite polarised electrode, they should be eliminated. A minimum needed voltage (V_{min}) is computed by adding all contributions:

$$V(j) = 1.23 \text{ eV} + \eta_{\text{anodic}}(j) + \eta_{\text{cathodic}}(j) + \eta_{\text{ionic cond.}}(j) \dots\dots\dots(3)$$

Record values of 1.4 V have been obtained for a current of roughly 10 mA•cm⁻².

1.8.5.6 Mechanism of water splitting on TiO₂:

Two basic processes, oxidation and reduction, occur as a result of water splitting. To generate H₂ and O₂, the positions of VB and CB of the semiconductor must fit inside the potential windows of water oxidation potential and reduction potential, respectively. When light falls on TiO₂, electrons which are present in the VB are lifted to the CB and holes are left behind. The creation of hydrogen is aided by excited electrons, while the generation of oxygen is aided by holes [112]. Because hydrogen is utilised as a fuel, it is critical to improve hydrogen generation. The addition of photosensitizers has been shown to significantly increase hydrogen generation.

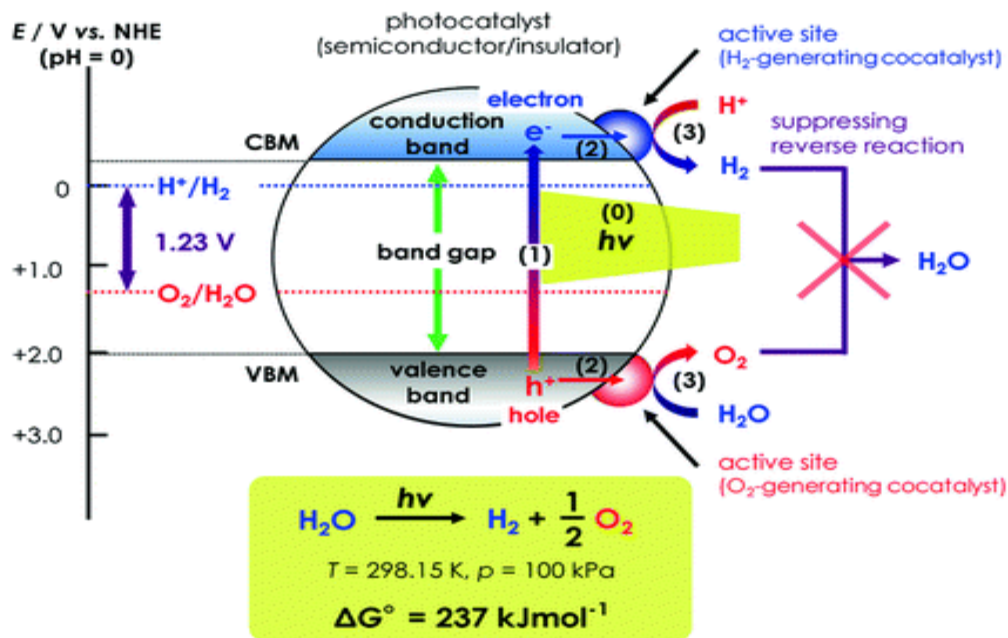


Figure 4 Photo-electrochemical water splitting cell with TiO₂ NTs as an n-type semiconductor

Ethylenediaminetetraacetic acid (EDTA) is a typical organic hole scavenger because it can readily be oxidised using the holes, allowing the CB electron to generate hydrogen. On certain typical hole scavengers, the ability to generate hydrogen is as follows: EDTA > methanol > ethanol > lactic acid. Because hydrogen is one of the results of the agents' decomposition, it can contribute to hydrogen production [61].

1.9 Aims & Objectives:

The important objective of this research work were;

To develop CoFe₂S₄/TiO₂ binary nanocomposite for photoelectrochemical water splitting.

- To synthesize high surface TiO₂ NTs
- To synthesize homogenous layer of CoFe₂S₄ over TiO₂ nanotubes
- To characterize the heterojunction using XRD, SEM-EDS, UV-Vis-DRS, Raman, FL and FTIR spectroscopy
- To check the photoelectrochemical water splitting using the heterojunction CoFe₂S₄/TiO₂ NTs

Chapter-02
Literature Review

Chapter_02

2. Literature Review:

To create TiO₂ nanotubes, Chin-Jung et al. utilised electrochemical anodization vertically on a Ti foil. They adjusted the water content (1, 3, and 6 wt percent) of the electrolyte in ethylene glycol in the presence of 0.5 wt percent NH₄F with anodization for various applied voltages (20-80 V), durations (10-240 min), and temperature to control the length of these TiNTs from 2.4 to 26.8 μm. (10-30°C). It has the maximum photocatalytic activity because to its length, geometry (wall thickness and surface roughness), and crystalline structure. The length was optimised, which resulted in a considerable outcome. Using ethylene glycol as an electrolyte, TiO₂ nanotubes were produced on Ti foil. For better photocatalytic performance, they looked into high-profile anodization factors such as anodization temperature, anodization time, applied voltage, and electrolyte water content. Characterization of the sample was done through Field emission scanning electron microscopy (FESEM), XRD, Solaronix adsorption measurement, and Uv-Vis spectroscopy. Higher the water content of an electrolyte, lower will be the length of the TiNTs. Also higher the applied potential of about 80V not more than that, gives a TiNTs with higher length and better surface roughness[37].

Bu Chen et.al studied that, TiO₂ nanopores are converted into nanotubes by increasing OH⁻ ion concentration, which may affect the nanotubes formation. Thus dehydration of titanium hydroxide from the walls leads to the formation of bamboo type nanotube, which shows

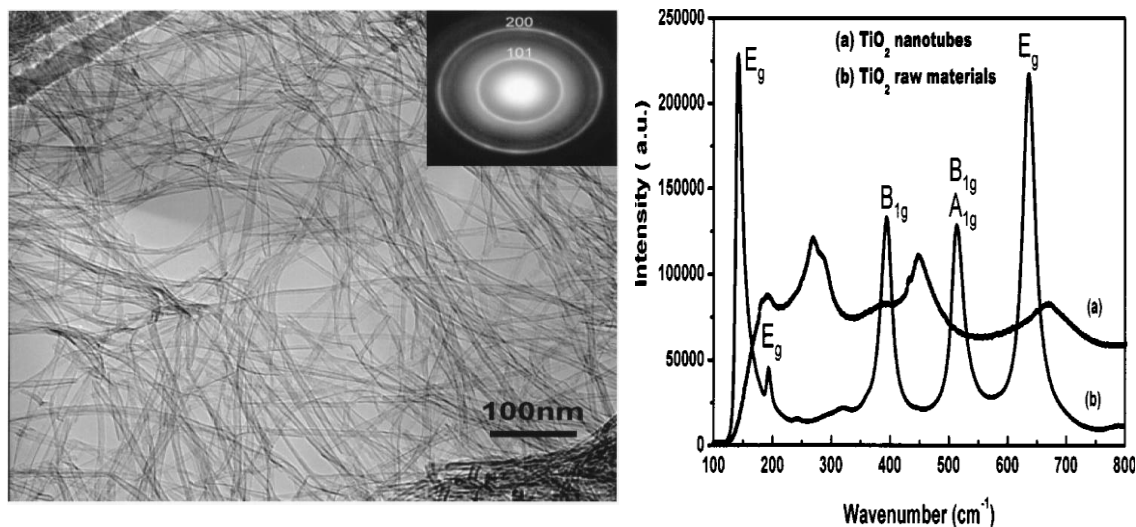


Figure 5 TEM images and Raman spectra of the as-prepared TiO₂ nanotubes

excellent splitting efficiency and supercapacitor performance. Besides four models were proposed for the tubular array of TiO₂ nanotubes; TiO₂ related devices is difficult to design, as mechanism for TiO₂ nanotubes formation is still ambiguous. By varying the temperature and time of the hydrothermal process, researchers were able to better understand the production process and mechanism of TiO₂ nanotubes. At various phases, TEM was employed to characterise the gathered samples.

According to transmission electron microscopy, TiO₂ nanotubes made utilising a simple hydrothermal chemical technique created a crystalline structure with an open-ended and multiwall shape. Along with SEM and FTIR, electrochemical impedance spectroscopy (EIS) was used to determine the structural evolution of TiO₂ nanotubes. [38].

M.A. Rahman and colleagues investigated the influence of anodization time on TiNT production. Nanotube diameter and length are directly related with anodization time. They looked at the oxidation of Ti foil in an electrolyte comprising NH₄F and (NH₄)₂SO₃ at a constant voltage. Titanium foils anodized at various times have well-ordered nanotubes of

various sizes. Calcination of fabricated nanotubes at 500 °C was used to investigate the crystal

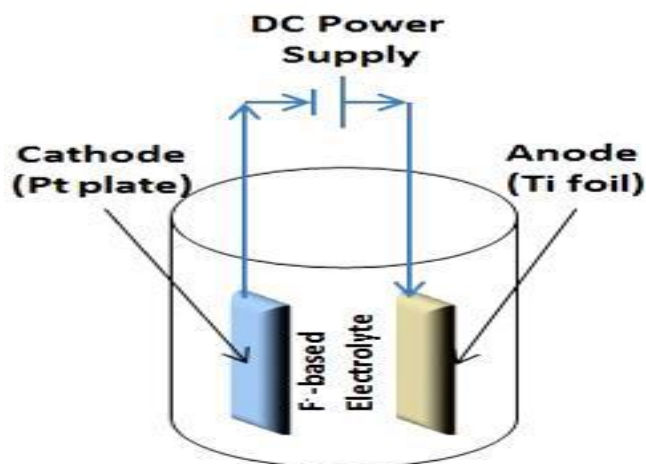


Figure 6. Experimental setup for Ti anodization

changes of TNT structures from amorphous to anatase, rutile, and brookite. X-ray diffraction was utilised to determine crystallinity and phase information, while scanning electron microscopy (SEM) and energy-dispersive X-ray spectroscopy (EDX) were used to analyse the morphology and chemical composition of the as-prepared nanotubes. Main disadvantages for anodization process is that we get an amorphous nanotubes which are converted to crystalline form by post heating, as a result stability of the tubes are disturbed, and eventually leads to the collapsing of the tubes[39].

TiO₂ and CNTs heterojunction membranes were produced by Chemical Vapor Deposition at 650 °C in an H₂/He environment, in which TiO₂ nanotubes were detached from Ti foil carrying TiNTs, according to Zohreh R. Hesabi et al. Ultrasonication, selective dissolving of the supporting Ti substrate, lowering the anodization voltage at the end of the anodization process, and the delivery of a big voltage pulse for a limited time are currently employed to remove TNT arrays from the Ti substrate. The findings of this work suggest that a heterojunction membrane made of TiO₂ nanotubes and carbon nanotubes could be developed in the future. The newly discovered heterojunction membranes are predicted to benefit water purification, water splitting, dye-sensitized solar cells, biofilters, desalination, sensors, and a range of other

applications. Glancing angle X-ray diffraction (GAXRD), Field Emission Scanning Electron Microscope (FESEM), and XPS are some of the characterization techniques used. [40].

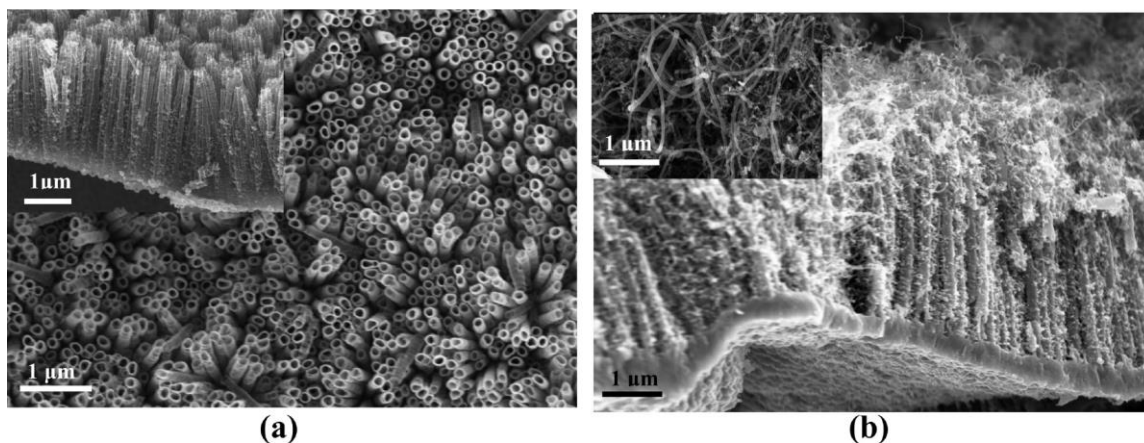


Figure 7. FESEM images at 680 °C (a) Before & (b) After

York R. Smith studied the array of TiO₂ nanotube on foil and wire substrate and found that over 40% increase in hydrogen production were observed for foil nanotube and over 25% were observed for nanotubes on wire. Photoelectrochemical response for untreated foil nanotube are; Photocurrent density 1.23mA/cm² at 1.23V, having open circuit potential (OCP) are 0.10 V. After etching the foil for 30s give the same result of PEC. When etching for 60 seconds, the current density increases by 13.8 percent to 1.40 mA/cm², however the OCP remains the same as when etching for 30 seconds. Photocurrent density for untreated wire is 1.47 mA/cm² at 1.23V with an OCP of 0.15 V. Now, etching this wire for 30 seconds causes a 20% increase in current density to 1.78 mA/cm², but etching for 60 seconds causes no additional increase in current density. At 0.3 V, wire-30 has a maximum efficiency of 1.84 percent, whereas at 1.23 V, it has a maximum efficiency of 0.35 percent. At 0.29 V, foil-60 has a maximum efficiency of 1.45 percent, whereas at 1.23 V, it has a maximum efficiency of 0.15 percent. Only SEM was used for characterisation. [41].

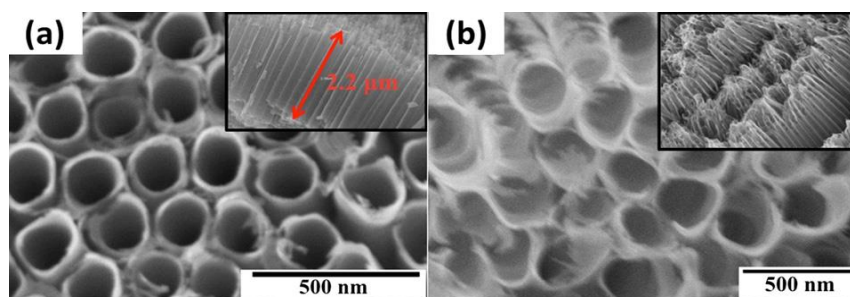


Figure 8 SEM images of TiO₂ nanotubes (a) wire (b) substrate

Lei Ma et.al studied that there is a decrease in the photocatalytic characteristics of the as prepared sample CNTs/Fe-Ni/TiO₂ due to an increase in reaction temperature of fluidized bed chemical vapor deposition (FBCVD). At low temperature say 500 °C, in 180 min, more than 90% and approximately 50% of methylene blue was degraded under visible light, with wavelength of 300 nm. (Chen, Cho, & Oh, 2010) Cr₂O₃-CNT/TiO₂ nanocomposites were prepared by solution method, but its major drawback is that CNTs have been altered by the use of strong acids or other similar chemicals, resulting in alterations in the graphitic structure of CNTs. Thus CNTs/Fe-Ni/TiO₂ were prepared using FBCVD, where Fe and Ni doped CNTs were developed on the TiO₂ NTs surface. FBCVD temperature is 500-550 °C, anatase content in C-FNT will be 100%, but when temperature is increased to 650 °C, then anatase content will be 20% only, thus rutile phase will occurs on 650 °C temperature. The catalytic centre for CNT production is doped Ni(II), which has been shown to be slightly reduced to the metal state. The photocatalytic activity of UV and visible light were assessed using the degradation of MB. The photocatalytic activity of CNTs/Fe–Ni/TiO₂ samples prepared at lower temperatures is higher than that of those prepared at higher temperatures. Furthermore, CNTs, Fe ions, and Ni, all of which are reduced in the FBCVD process, are thought to have a synergistic effect on photocatalytic activity. The CNTs and Ni may act as the photo-generated transfer bridge and the CNTs may act as the absorbent in CNTs/Fe–Ni/TiO₂ composite photocatalysts. The TiO₂ band gap narrows as a result of Fe ions, allowing more light to pass through to the visible region. Characterization techniques include FESEM, XRD, BET, Raman Spectroscopy, TEM, XPS, UV Visible Spectroscopy, and XPS. [42].

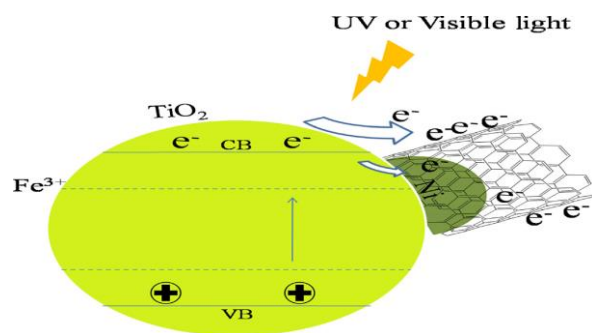


Figure 9 Photocatalytic activity mechanism in CNTs/Fe–Ni/TiO₂.

M.Misra et.al deposited multi-walled Carbon nanotube (MWCNTs) on nanoporous titanium dioxide (TiO₂) template. Ti foil was utilised as an anode and platinum was employed as a cathode during the anodization process. After applying potential to the electrodes, the anodization current between the two electrodes were recorded by the software, “Picolog Recorder”, which directly connect the rectifier to the computer and plot the graph as the experiment proceeds. During Cobalt deposition on TiO₂ nanotube, the current density of cathode were (-) 70 mA/cm² and that of anode were (+) 70 mA/cm². During the anodization color change were also observed according to anodization time. At 1sec, the color were deep violet, at 10 sec it were violet, then 50 sec, 75 sec and in last at 2700 sec it were shiny pale orange, all were due to the multiple beam interference while striking the TiO₂ surface. At the start of anodization, current peak were high, which drop back to a much lower value 0.8mA/cm²-0.9mA/cm², and then increase to ~1.24mA/cm² and remain constant, which might be because of the removal of the layer of oxide from surface of titanium left after pretreatment. Cobalt is used as catalyst and is deposited using PED technique. We believe that the synergistic approach of using anodized titanium and carbon nanotubes on the titanium oxide substrate will have far reaching utilization in developing emitters, composites, devices, and robust sensor technologies in the future. Characterization technique are SEM, TEM , EDS, XPS, GXRD and ED[43].

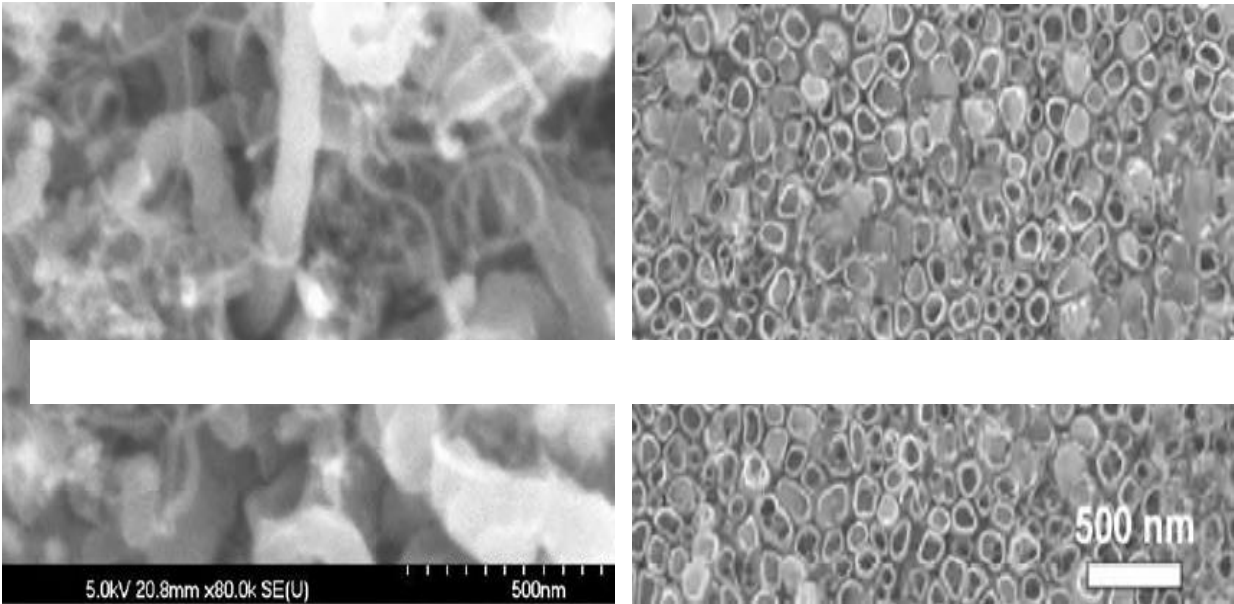


Figure 10 FESEM micrograph of an ultrasonicated MWCNT-Co-TiO₂ material (a) for 1 min and (b) for 45 min.

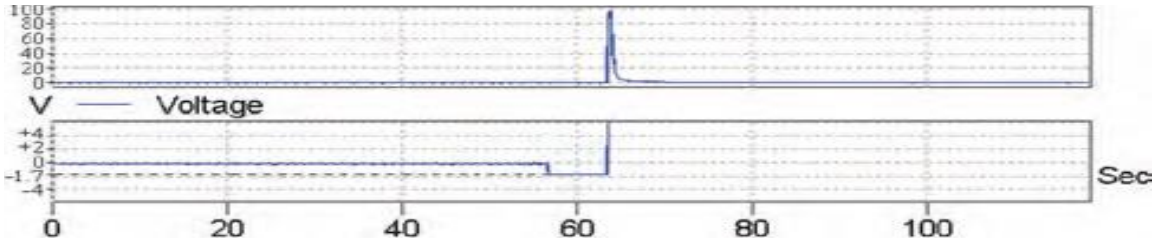


Figure 10. The voltage drop from zero to -1.7 V before anodization.

A. Ali and W. Oh, degraded Reactive Black B (RBB) dye by using synthesized CoS₂-G-TiO₂ nanocomposite through micro-wave assisted techniques under visible light. Photodegradation of RBB dye by TiO₂-G, CoS₂-G, and CoS₂-G-TiO₂ nanocomposite after 180 min are 37%, 53% and 89% respectively. The excellent performance by the nanocomposite is because of the homogenous distribution of CoS₂ and TiO₂ on Graphene surface. When bombarded with visible light, the CoS₂-G-TiO₂ ternary nanocomposite may clearly be used as a capable photocatalyst. This exceptional photocatalytic activity is due to the positive synergistic effects

of CoS₂, TiO₂, and graphene. SEM and TEM images revealed that CoS₂ was consistently spread over graphene sheets supported by TiO₂ nanoparticles. A considerable reduction of GO to rGO, as well as the existence of CoS₂ and TiO₂ anatase crystal phase can be clearly seen by XRD and Raman spectra. Characterization techniques used were XRD, TEM, SEM, UV-Vis spectroscopy and Raman spectroscopy [44].

Sivagowri Shanmugaratnam and colleagues created a CoS₂/TiO₂ nanocomposite. After materials have been synthesised using a hydrothermal approach, the hydrogen generation efficiency of pure CoS₂, TiO₂ nanoparticles, and CoS₂/TiO₂ nanocomposites is compared under UV irradiation. 10 wt % CoS₂/TiO₂ nanocomposites produce more hydrogen (2.55 mmol g⁻¹) than pristine TiO₂ nanoparticles, but pristine CoS₂ nanoparticles produce no hydrogen. The metal dichalcogenide–CoS₂ serves as an effective co-catalyst by successfully separating the photogenerated electron–hole pair, while nanocrystalline TiO₂ serves as an active site. As a characterisation approach, PXRD, SEM, and UV-Vis DRS were used. [45]. Finally, hydrogen production appears to be influenced by the band gap energy of the catalysts, and CoS₂ may aid in successfully separating the electron-hole pair forms in the mixed nanocomposite, resulting in a higher hydrogen production value.

Material	Synthesis Method	Rate of Hydrogen Evolution	Sacrificial Agent	Reference
2D SnS ₂ /g-C ₃ N ₄ (5 wt.% SnS ₂ /g-C ₃ N ₄)	Hydrothermal method	0.97 mmol h ⁻¹ g ⁻¹	10 vol% TEOA and 3 wt.% H ₂ Pt ₂ Cl ₆ ·6H ₂ O	Enzhou Liu et al., 2018
Te/SnS ₂ /Ag	Hydrothermal method	0.33 mmol h ⁻¹	-	Changzeng Yan et al., 2017
SnS ₂ Nanosheets	Solvothermal	1.06 mmol h ⁻¹ g ⁻¹	0.1 M Na ₂ S 0.1M Na ₂ S ₂ O ₃	Jing yu et al., 2014
CdS/ WS ₂	Impregnation-sulfidation	0.42 mmol h ⁻¹	Latic acid solution	Zong et al., 2011
Dye-Sensitized NiS _x / graphene (in EY/G)	Insitu chemical deposition method	0.04 mmol h ⁻¹	-	Chao Kong et al., 2014
Dye-Sensitized NiS _x / graphene (in EY/NiS _x /G)	Insitu chemical deposition method	0.34 mmol h ⁻¹	-	Chao Kong et al., 2014
MoS ₂ / RGO and CdS (pH11-MoS ₂ /rGO 1.5/CdS)	Photoreduction method	0.10 mmol h ⁻¹	10 vol.% Latic acid solution	Yuexiang Li et al., 2014
MoS ₂ /Graphene	Hydrothermal	1.80 mmol h ⁻¹	Na ₂ S-Na ₂ S ₂ O ₃ solution	Chang et al., 2014
MoS ₂ quantum dots/TiO ₂ nanotube arrays	Electrodeposition	0.07 mmol cm ⁻² h ⁻¹ 0.05 mmol cm ⁻² h ⁻¹ 0.02 mmol cm ⁻² h ⁻¹	-	Qun Wang et al., 2018
ZnTCPP-MoS ₂ /TiO ₂ (1.00 wt.% MoS ₂ on TiO ₂)	Hydrothermal	0.10 mmol h ⁻¹	0.2 M triethanolamine (TEOA) aqueous	Youngjun Yuan et al., 2015
10 wt.% CoS ₂ /TiO ₂	Hydrothermal	2.55 mmol g ⁻¹	Methanol	This work

Figure 11 A comparison between different chalcogenides metals for hydrogen evolution

Seung Wook Shin et al. used electrochemical anodization followed by sulfurization on a Ti substrate to generate and analyse sulphur (S)-doped TiO₂ nanotubes (TONTs).

For the production of S-doped TONT arrays, annealing temperatures ranging from 450 to 550 °C were given for 10 minutes. The synthesis was carried out in the presence of H₂S gas, and no differences in morphological qualities were observed when compared to the TONT arrays. The 500 °C annealed S-doped TONT arrays had higher electric conductivity and greater visible light absorption in the 0.1 M KOH solution, resulting in the maximum photocurrent

density (2.92 mA cm² at 1.0 V vs sat. Ag/AgCl) as compared to TONT arrays (0.965 mA cm² at 1.0 V vs sat. Ag/AgCl). In the UV, incident photon-to-electron conversion efficiency (IPCE) of S-doped TONT arrays was around 43%, whereas TONT arrays exhibited a 32 percent IPCE. Furthermore, the S-doped TONT arrays had poor photoactivity in the visible light range up to 600 nm wavelength at 500 nm, with an IPCE value of 2.4 percent, compared to the TONT arrays' inconsequential IPCE values. Due to the emergence of rough tube morphological properties, defective regions in the edge of TONT arrays, and the passivation impact in the interface between S-doped TONT arrays and water and defective regions, excessive S doping in TONT arrays reversed the reduced photocurrent (2.04 mAcm⁻² at 1.0 V vs. sat. Ag/AgCl). The PEC efficiency was increased by optical, electrical, and crystalline properties change as a result of the appropriate inclusion of foreign contaminants in the TONT arrays[46].

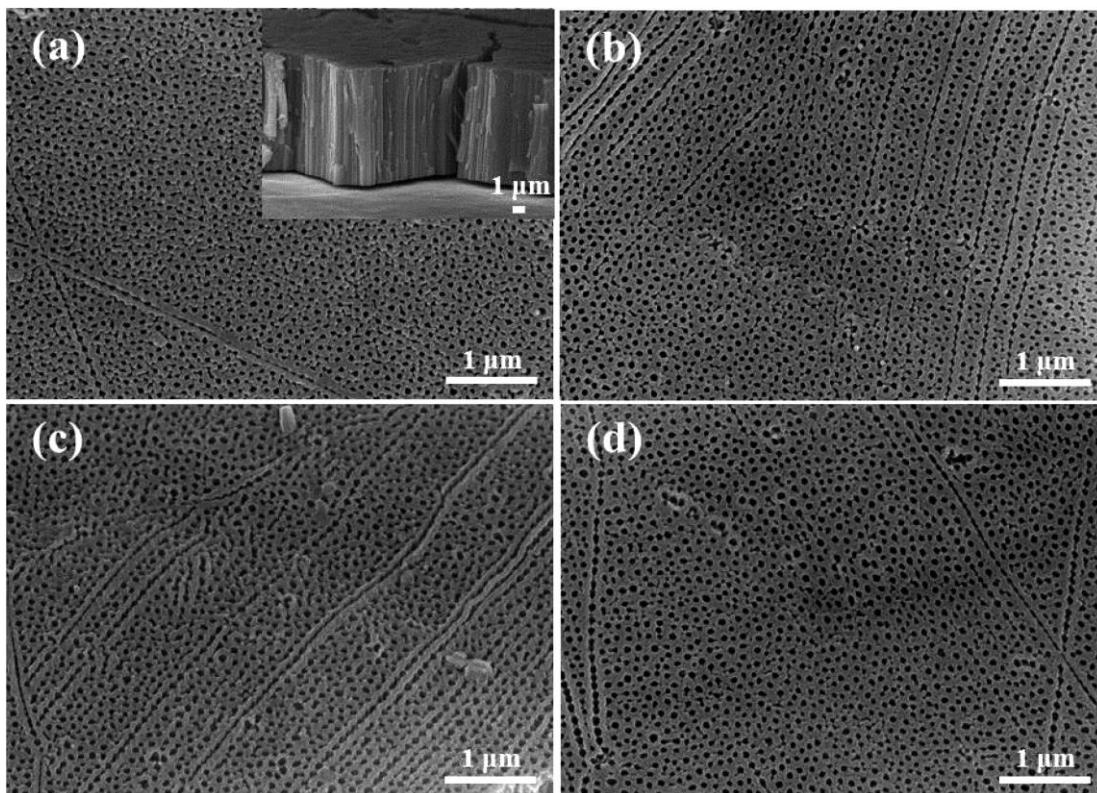


Figure 12 FE-SEM images of (a) TONT film, (b) the S-doped (450 °C) (c) 500 °C and (d) 550 °C

Di-Yan Wang et al. have developed a photoelectrochemically useful semiconducting nanocomposite that is abundant on Earth. As a photoanode, titanium oxide and iron pyrites are combined in this nanocomposite. The techniques used to characterise the atomic composition and detailed structure of the prepared $\text{FeS}_2/\text{TiO}_2$ photoanode included powder X-ray diffraction (XRD), energy dispersive X-ray spectroscopy (EDS), high-resolution transmission electron microscopy (HRTEM), Raman spectroscopy, and inductively coupled plasma with atomic emission spectroscopy (ICPAES). The photoanode $\text{FeS}_2/\text{TiO}_2$ displayed a high photoresponse from visible light stretched to the near IR range (900 nm) as well as a four-hour endurance test. Surface imperfections in FeS_2 were removed, and charge transfer at the $\text{FeS}_2/\text{TiO}_2$ interface was increased, both of which were proven to be critical factors in increasing photoresponse.

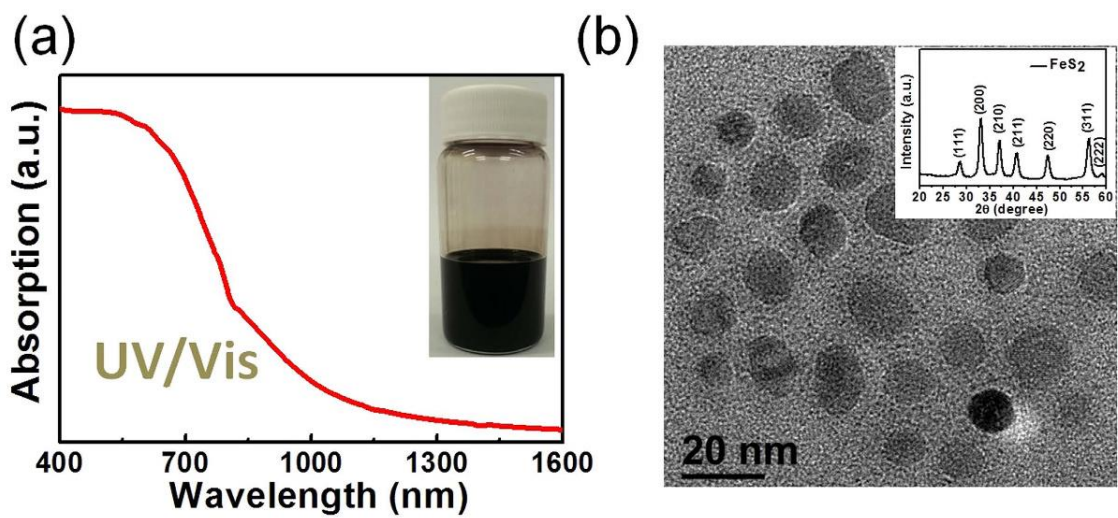


Figure 13 (a) Absorption spectrum & (b) TEM image of FeS₂ NCs.

This research showed that the FeS₂/TiO₂ photoanode, which is made up of earth-abundant elements, has very strong photo sensitivity in the visible to near-infrared region and can generate hydrogen by PEC. In the PEC application, the surface imperfection of FeS₂ was discovered a crucial parameter affecting the light response shown by FeS₂/TiO₂ photoanode. In order to remove FeS₂ surface defects and improve the interface charge transfer between FeS₂ and TiO₂, appropriate sulfurization was used. We considered that this work indicated not only a breakthrough in the utilization of FeS₂ as photoanode materials to generate hydrogen from visible to near-infrared radiation, but also a one-of-a-kind answer to the development of sulfur-based binary materials for PEC applications. [47].

Yanmei Xin et al. demonstrated that by coupling air and solution stable pyrite iron disulfide (FeS₂) nanotubes (TiO₂ NTs) with hierarchical bottom-tubular-top-porous TiO₂ nanotubes (TiO₂ NTs) with photocurrent enhancement of 3 times more than pristine TiO₂ nanotubes (TiO₂ NTs) with photocurrent enhancement of 3 times more than pristine Ti. The remarkable improvement in PEC performance can be attributed to the sensible combination of FeS₂ with a small band gap and TiO₂ NTs with a unique shape and acceptable electrical characteristics.

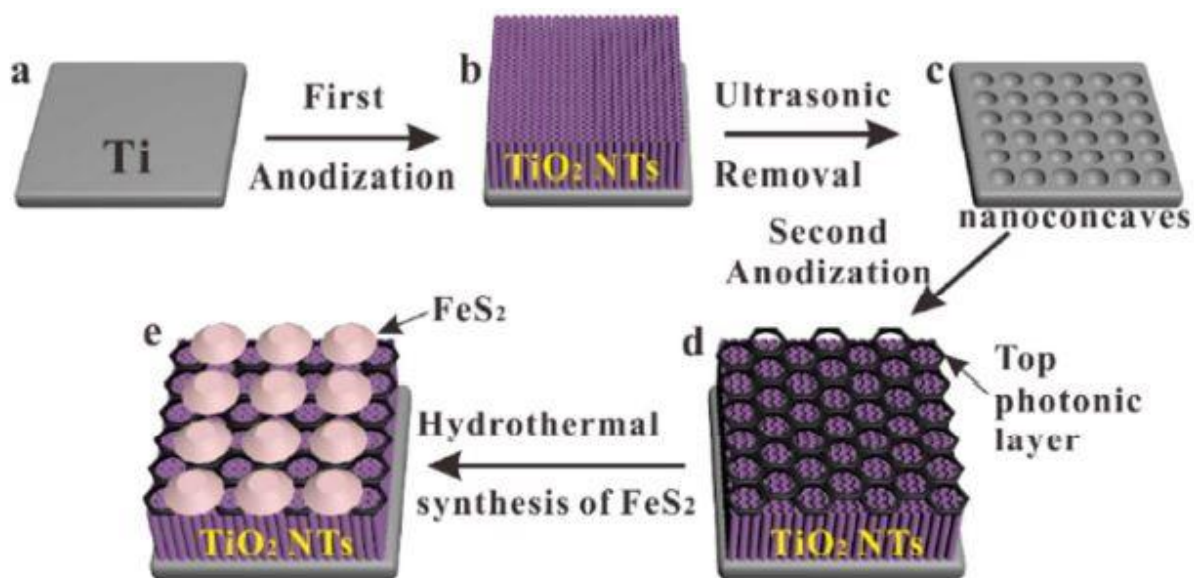


Figure 14 Synthesis procedure of FeS₂/TiO₂ NTs. (a) Ti foil, (b) first anodized TiO₂ NTs, (c) nanoconcaves (d) second anodized TiO₂ NTs and (e) FeS₂/TiO₂ NTs.

SEM, XRD, TEM, Raman and UV-Visible spectroscopy were used for the characterization of samples. Under the irradiation of solar light, infrared light responsive FeS₂ linked TiO₂ NTs with a top-photonic-layer bottom-tubular structure showed good PEC water splitting performance. [48].

Ibrahim Khan and A. Qurashi successfully fabricated an Ag/-Fe₂O₃/TiO₂ heterostructure using electrochemical anodization combined with another approach, pulse sonication. When silver (Ag) was put on -Fe₂O₃/TiO₂, the physical properties revealed a layered distribution of -Fe₂O₃ nanoparticles (NPs) over the TiO₂ nanotube arrays (NTAs), while Ag was pseudo-cubical. XRD patterns and X-ray photoelectron spectrometer (XPS) investigations revealed the growth of Fe₂O₃ and anatase TiO₂ crystalline phases, as well as the Ag/-Fe₂O₃/TiO₂ heterostructure. DRS UV-Vis spectroscopy revealed a steady decrease in the band gap with enhanced absorption in the visible portion of the spectrum due to the production of optically active heterostructures in the order Ag/-Fe₂O₃/TiO₂ (470 nm) > -Fe₂O₃/TiO₂ (424 nm) > TiO₂ (386 nm). In the DRS absorption spectra of Ag/-Fe₂O₃/TiO₂, the plasmon shoulder of Ag at 420 nm can be noticed. The photocurrent density of Ag/-Fe₂O₃/TiO₂ (2.59 mA/cm²) is nearly 2.5 and 5 times higher than that of -Fe₂O₃/TiO₂ (1.05 mA/cm²) and pristine TiO₂ (0.54

mA/cm²), respectively, due to Ag's plasmonic activity and -Fe₂O₃'s narrower band gap. Furthermore, electron impedance spectroscopy (EIS) indicated simple charge transfer in the same order as UV-Vis spectroscopy. These results demonstrate that the in situ electrochemical technique can be utilised to build customisable heterostructures for solar-driven water splitting. FESEM, SEM, EDX, UV-Vis-DRS, XPS, FTIR, and XRD were utilised as characterisation techniques. [49].

Table 1 Summary of some basic nanocomposite (Heterostructure)

Samples Composition	Method of synthesis	Electrolyte used	Light source	Current density	References
				J (mAcm⁻²)	
S doped TiO ₂ NTs	Anodization & Sulfurization	0.1 M KOH	Visible AM 1.5 light	2.94	[46]
FeS ₂ /TiO ₂ /FTO photoanode	Sol-gel & hydrothermal method	0.35 M Na ₂ SO ₃ and 0.24 M Na ₂ S	NIR continuous laser (808nm)	5.8	[47]
FeS ₂ /TiO ₂ NTs	Two-step Anodization, Hydrothermal	Phosphate buffer saline (PBS, PH = 7.4)	300 W Xe lamp with AM 1.5G filter	0.917	[48]
Ag/ α -Fe ₂ O ₃ /TiO ₂ NTs	Anodization process supported with pulse sonication	Na ₂ SO ₄ with 0.5 M (PH = 7.0)	Solar simulator with AM-1.5 G	2.59	[49]

Using a mild two-step hydrothermal method, Kun Song et al. created a novel hierarchical CoFe₂Se₄@CoFe₂O₄ and CoFe₂S₄@CoFe₂O₄ core-shell nanobox electrode. This electrode was utilised for the purpose of high-performance electrochemical energy storage. Because of the multifunctionality and core-shell structural advantage of the CoFe₂Se₄@CoFe₂O₄ and CoFe₂S₄@CoFe₂O₄ nanoboxes, novel hierarchical CoFe₂Se₄@CoFe₂O₄ core-shell nanoboxes electrode arrays with uniform size and morphology have been successfully deposited on nickel foam through a mild two-step hydrothermal method, and have been further developed

as binder-free electrode. In addition, at 1 A g^{-1} the $\text{CoFe}_2\text{Se}_4@ \text{CoFe}_2\text{O}_4$ electrode has a greater specific capacitance of 2040.8 F g^{-1} and outstanding throughput compared to other ternary transition metal sulphides. In addition, an asymmetric device with carbon nanotubes as the negative electrode, $\text{CoFe}_2\text{Se}_4@ \text{CoFe}_2\text{O}_4$ as the positive electrode, and 3 M KOH as the electrolyte shows a wider voltage range of 1.6 V, a desirable specific capacitance (463.27 F g^{-1} at 1 A g^{-1}), and a higher energy density of $164.72 \text{ Wh kg}^{-1}$ (at 508 W kg^{-1}) than other reviews. Moreover, the $\text{CoFe}_2\text{Se}_4@ \text{CoFe}_2\text{O}_4/\text{CNTs}$ asymmetric supercapacitor can operate a toy vehicle for more than 15 metres, suggesting the electrode's tremendous energy storage capability as well as its application potential [50].

Xinling Wang et al. developed a CFO/CFS/MBO ($\text{CoFe}_2\text{O}_4/\text{CoFe}_2\text{S}_4/\text{MgBi}_2\text{O}_6$) magnetic fibres (MNFs) photocatalyst for water disinfection using a simple hydrothermal technique. When the proper dosage of CFO/CFS/MBO was 0.5 mg/mL , the bactericidal rate against Methicillin-resistant *Staphylococcus aureus* was 99.8% after 60 minutes of visible light irradiation, as expected. The optimal sample (30% CFO/CFS/MBO composite) can breakdown 82.7 percent Cefotaxime sodium in 60 minutes (CTX). Under visible light irradiation, the ROS generated by the CFO/CFS/MBO photocatalyst was observed to cause severe damage to bacterial cell membranes and the degradation of antibiotic molecules. Due to the p-n-p heterojunction structural characteristics and abundant oxygen vacancies, CFO/CFS/MBO exhibited a larger absorption capacity of visible light and better photo-generated carrier separation efficiency, which had a startlingly good impact on the ability of photo-generated ROS. PL and EIS were used to improve the separation efficiency of photogenerated carriers. The transitional product, photodegradation pathway and active species in the photocatalytic process were confirmed using EPR, LC-MS analysis and scavenger studies. These CFO/CFS/MBO MNFs photocatalysts, which are extremely efficient and recyclable, could be used in wastewater treatment. A suitable reaction mechanism for photocatalytic water disinfection is proposed. The findings of this study are anticipated to serve as a blueprint for the creation of composite photocatalysts that combine

compact heterojunctions with oxygen vacancies to improve photocatalytic water disinfection. [51].

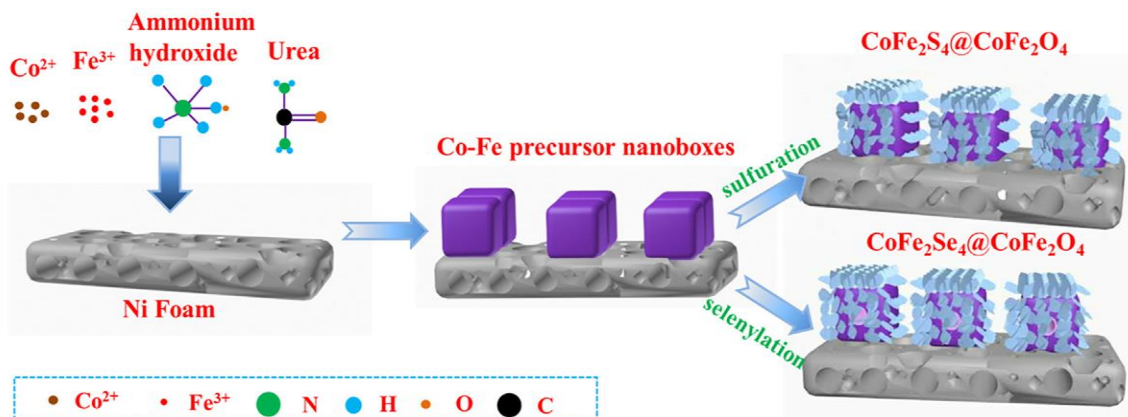


Figure 15 Formation of core-shell nanoboxes arrays on Ni foam.

Pranav Kulkarni and colleagues created nanostructured binary and ternary metal sulphide for energy conversion and storage. Redox reversibility, conductivity, and capacitance are all fascinating properties of metal sulphides. Binary metal sulphides have also gotten a lot of attention since they have a lot of redox reaction sites and have a lot of electrical conductivity when compared to metal sulphides. Different researchers have recently investigated the use of binary metal sulphides as electrode materials for a variety of applications, including lithium-ion batteries (LIBs), solar cells, and supercapacitors (SCs). This review aims to provide an analytical overview of the approaches and advancements gained in generating better results from these sulphides in order to chart a course for scale-up and provide long-term solutions to the energy and environmental challenges. Finally, the research scope for metal sulfide-based energy materials was highlighted, as well as the challenges to achieving great performance. [52].

Phosphorus doped cobalt-iron sulfide/carbon nanotubes were created by Ling Huang et al. as an effective as well as durable electrocatalyst for splitting of water. Using a combination of Co and P co-doping, hybridization with carbon nanotubes (CNTs), and nanostructuring, we show that the suggested CoFeSP/CNT with optimal composition is an enhanced bifunctional

electrocatalyst for hydrogen and oxygen evolution events. When utilised as a hydrogen evolution electrode, the as-synthesised CoFeSP/CNT are active and stable in both alkaline and acidic electrolytes. Low overpotentials of 262 and 309 mV were observed at current densities of 10 and 100 mA cm⁻², respectively, from in-situ electrochemically generated CoFe-oxyhydroxides, indicating good performance as oxygen-evolution electrodes. A two-electrode alkaline water electrolyzer constructed with three-dimensional CoFeSP nanorods on carbon cloth (CoFeSP/CC) can also deliver a current density of 50 mA cm² at 1.62 V. To characterise the generated nanocomposite, HR-TEM, SEM-EDX, XRD, Raman, and XPS were used. [53].

Mengjiao Gao et al. in-situ built nanoflakes made of CoFe₂O₄ and CoFe₂S₄ on nickel foam (CFS-10/NF) via a surface sulfidation alteration. To establish the composition and structure, researchers used a variety of methods, including transmission electron microscopy and an X-ray diffractometer. When employed as a free-additive electrode material, the 3D CFS-10/NF sample showed outstanding capacity (4.6 F cm⁻² at 1 mA cm⁻²), good rate capability, and consistent cycling performance. An asymmetric supercapacitor device using CFS-10/NF as anode and activated carbon as cathode displayed improved performance, with a high areal capacitance of 190.5 mF cm⁻² and an energy density of 19.8 W h kg⁻¹. After 3000 cycles, 100 percent capacity was still there, demonstrating good cycling stability. Due to its rich redox reaction and high electrical conductivity boosted by well-designed composition, as well as large specific surface area and short ions transit path attributed to nanoflake structure, the composite material has a lot of potential in energy storage applications. The material performs well despite its high iron content, thanks to a large specific surface area and highly effective ions diffusion path derived from the nanoflake structure, as well as a reinforced synergic effect and enhanced electric conductivity due to the complementary composition of CoFe₂O₄ and CoFe₂S₄, implying that iron-rich materials have a promising future in energy storage. [54].

Chapter-03
Materials & Methods

Chapter-03

3. Materials & Methods:

3.1 Materials:

Titanium foil (99.5%, with thickness 0.127 μm , Sigma-Aldrich), NH_4F (practical grade, Duksan, Korea), Ethylene glycol (99.5%, Sigma-Aldrich), Thiourea (99.7%, Sigma-Aldrich), Iron (III) nitrate nonahydrate (above 98% extra pure, Korea), Cobalt (II) chloride hexahydrate (Laboratory reagent grade), Sodium sulfite anhydrous (extra pure, 96%, Korea), Hydrofluoric acid (99.98%, Sigma-Aldrich), De-ionized water (ultra-pure), Ethanol (99%, Analytical grade), Acetone (99+%, Analytical grade). All were analytical grade and were used as received i.e without extra-purity.

3.2 Apparatus:

Beakers, Magnetic stirrer, pipette, graduated cylinder, Wash bottle, Petri-dish, syringe, China dish etc were used. All the apparatus were cleaned through DI-water before using in the process.

3.3 Instruments & Equipments:

Digital balance, Ultra-sonicator, hot-plate, vacuum oven, muffle furnace, tube furnace and thermal gun were used in the whole synthesis.

3.4 TiO_2 nanotubes synthesis

Pure Titanium foil of thickness 0.127 μm was used to prepare TiO_2 (Titania) nanotubes array using the anodization method. Before anodization, Ti-foil was mechanically cut into ($1 \times 1 \text{ cm}^2$) rectangular shape and were chemically etched in a dilute solution of hydrofluoric acid for 30 sec, and afterward, were rinsed with deionized water. Titanium foil was then mechanically polished with low-quality Silicon Carbide (Abrasive) paper. Thereafter, they

were cleaned in an ultrasonic bath using acetone, ethanol, and DI-water sequentially for 15 mins and then dried in air.

The anodization was performed in a two-electrode cell, where the cleaned Ti-foil was pressed against an O-ring and used as the anode, while a platinum ring was used as a cathode. A two-centimeter distance was maintained between the anode and the cathode. Ethylene glycol was used as an electrolyte containing 0.5 wt% NH_4F and 3 vol% DI-water. All the process of anodization was conducted at room temperature, under 30 V anodization voltage, for 3 hours using DC-power supply (GPC-30300). After that, amorphous titania was rinsed with ethanol and DI water for the removal of surface impurities. Finally, the samples were heated by 15 $^{\circ}\text{C}/\text{min}$ rate in a tube furnace to 450 $^{\circ}\text{C}$, for 2 hours to get crystalline TiO_2 NTs and then cooled to room temperature before characterization.

3.5 CoFe₂S₄/TiO₂ nanotubes synthesis:

The obtained TiO_2 nanotubes array were dipped in a mixed 25 mM solution of cobalt (II) chloride hexahydrate ($\text{CoCl}_2 \cdot 6\text{H}_2\text{O}$) and 50 mM $\text{Fe}(\text{NO}_3)_3 \cdot 9\text{H}_2\text{O}$ (iron (III) nitrate nonahydrate) solution with a SILAR technique. The beaker was kept in a vacuum oven for 3 minutes each time to remove air bubbles inside the nanotubes so that Co^{+2} and Fe^{3+} ions go inside the tube properly. TiO_2 nanotubes plates were then rinsed in DI-water to washout extra surface cations. Finally, the samples were put at hot-plate to dry at 250 $^{\circ}\text{C}$ temperature. The aforesaid procedure was considered as one SILAR cycle. As to check the various loading-activity of $\text{CoFe}_2/\text{TiO}_2$ nanotubes, the number of SILAR cycle for Co^{+2} and Fe^{+3} ions adsorption were performed ranging from 05 to 20 cycles.

Chemical vapor deposition (CVD) was performed finally in tube furnace using Thiourea as a sulfur precursor to synthesize $\text{CoFe}_2\text{S}_4/\text{TiO}_2$ nanotubes. Initially, Co^{+2} & Fe^{3+} adsorbed at TiO_2 NTs were reduced in the presence of Argon & H_2 gas to form $\text{Co}^0\text{Fe}^0/\text{TiO}_2$ NTs. During reduction, Ar-gas were allowed to flow by setting ramping temperature of 20 minutes to obtain the temperature of 400 $^{\circ}\text{C}$. The reaction stay at 400 $^{\circ}\text{C}$ temperature for 60 minutes, then H_2 gas was passed through the furnace. $\text{Co}^0\text{Fe}^0/\text{TiO}_2$ NTs were oxidized in the presence of thiourea to get $\text{CoFe}_2\text{S}_4/\text{TiO}_2$ NTs. During oxidation, $\text{Co}^0\text{Fe}^0/\text{TiO}_2$ NTs foils were

placed against Thiourea and the reaction temperature were carried up to 300 °C in ramping temperature of 10 minutes and maintained that temperature for 30 minutes, and again in 30 minutes the reaction temperature reached 450 °C and stay there for 30 minutes. Thus it was observed that $\text{Co}^0\text{Fe}^0/\text{TiO}_2$ NTs, was sulfurized in thiourea to form $\text{CoFe}_2\text{S}_4/\text{TiO}_2$ NTs. Various loading cycles were 05- $\text{CoFe}_2\text{S}_4/\text{TiO}_2$ NTs, 10- $\text{CoFe}_2\text{S}_4/\text{TiO}_2$ NTs, 15- $\text{CoFe}_2\text{S}_4/\text{TiO}_2$ NTs and 20- $\text{CoFe}_2\text{S}_4/\text{TiO}_2$ NTs respectively.

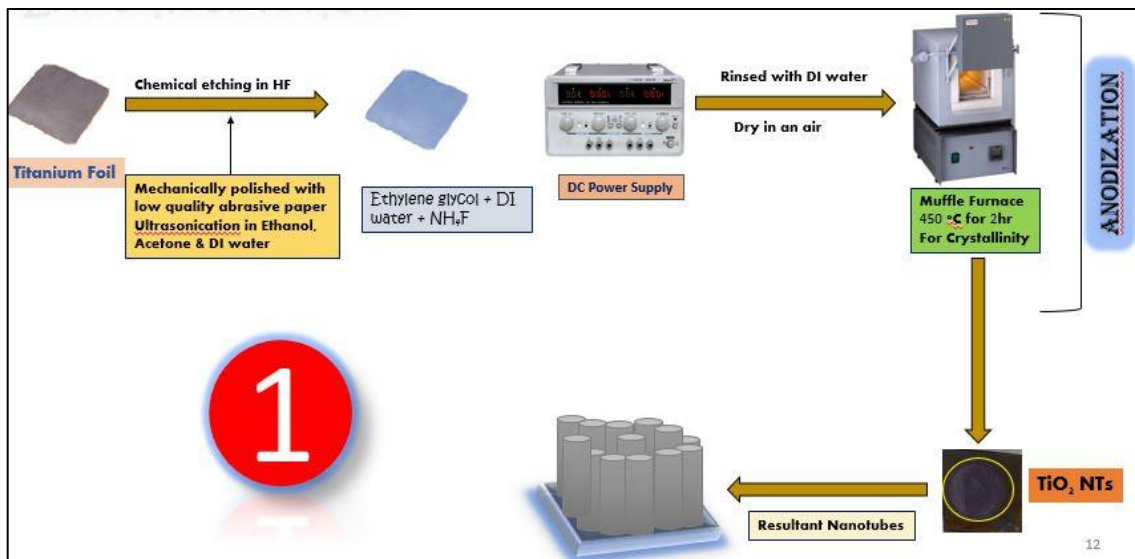


Figure 17 Schematic diagram for anodization process.

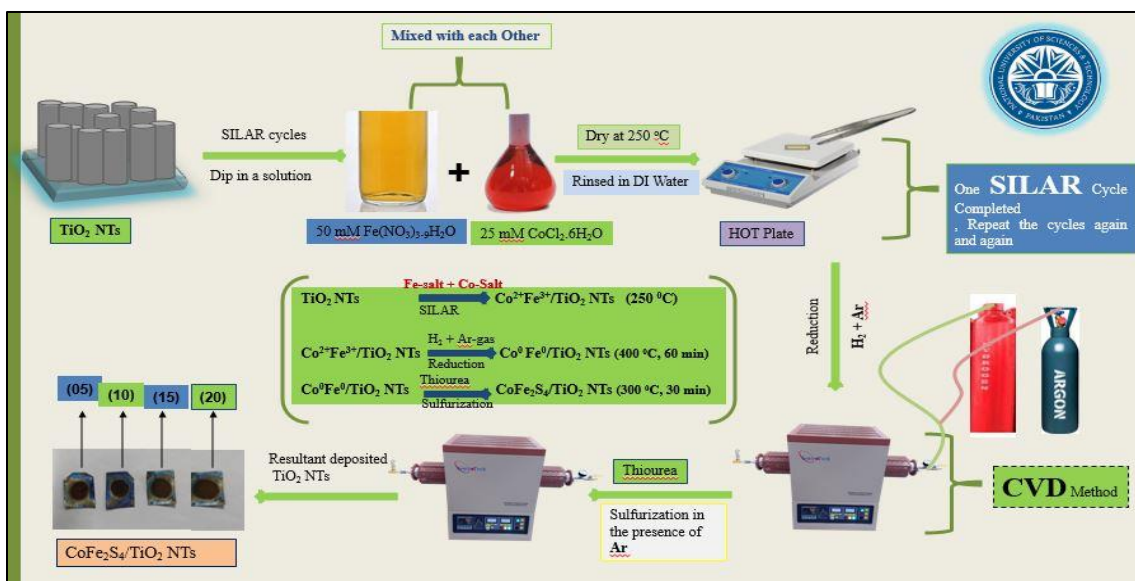


Figure 16 Schematic diagram for SILAR cycle and CVD technique.

3.6 Characterization:

Crystalline structure and phase identification of FeS-FeS₂/TiO₂ nanotubes was done using X-ray diffraction (XRD; Bourestnik dron 8 PXRD) with an excitation wavelength of ($\lambda = 1.5405 \text{ \AA}$) in the range of 10-80°. To observe the nanostructured morphology of a sample and to do its elemental study, Scanning Electron Microscopy (SEM, JSM-6490) as well as Energy-Dispersive X-ray Spectroscopy (EDS, VEGA3 LMU) were used respectively. UV-Vis Diffuse Reflectance spectra were measured with PerkinElmer UV/Vis Lambda 365, between the wavelength of 300-800 nm. The Raman scattering analysis was performed (Renishaw 2000 spectrometer) with the incident wavelength of 633 nm to determine Raman vibrational modes of the photocatalyst. Fourier transform infrared spectroscopy (FTIR; Bruker FTIR alpha) was used to determine various functional groups and their stretching or bending vibrations in a functional group or fingerprint region in the range of 4000-500 cm⁻¹. Photoluminescence spectroscopy (PL; PerkinElmer Fluorescence Spectrometer, FL-6500) was performed to determine the excitation-emission spectra at 400 nm excitation wavelength.

3.6.1 Introduction to characterization techniques:

Characterization of the material for particular application is immensely necessary. Without proper and prior knowledge of the material size, shape, morphology, crystal structure and elemental analysis, applications and activity of the material is of no need. For this purpose to get know about all the aforesaid parameters about the material, a number of characterizations have been done. All of those in detail will be explain in the following paragraphs of this chapter.

3.6.1.1 X-ray Diffraction:

The first and foremost imperative characterization technique is XRD to find the crystal structure and crystallinity in a material. Determining the orientation of an atom or grain in a crystal lattice or structure and the separation between different planes from which material are consisted of. Furthermore, with the help of this technique the size, and the internal stress in the crystalline structure could be obtained.

3.6.1.2 Scanning Electron Microscopy (SEM):

For multiple type of signal generation at the samples surface, a high-energy electron focused beam is used by electron scanning microscope (SEM). The signals from secondary electrons (SE) and backscattered electrons (BSE) are studied and claimed. Various sample information like chemical composition, morphology of surface, crystalline structure etc. are revealed with the help of SEM. On predefined areas of the sample surface, the beam is scanned and collection of data is performed.

3.6.1.3 Raman Spectroscopy:

Raman spectroscopy is an additional characterizations used to find the vibrational modes present within a molecule. Besides vibrational modes, rotational mode and other low energy modes can also be find out. Raman spectroscopy is a nondestructive technique that is used to obtain chemical structure information, crystallinity, polymorphy molecular interactions and phase of the molecule. The basic principle of raman spectroscopy is the interaction of laser light with the chemical bonds present within a molecule.

3.7 Photoelectrochemical measurement:

To determine the photoelectrochemical ability of all the prepared samples, photoelectric studies were performed using Potentiostat/Galvanostat/ZRA (Model; INTERFACE1000E-12095) in a three-electrode setup with FeS-FeS₂/TiO₂ nanotubes (various loading) as a working electrode with 0.282 cm² active exposed surface area, a Pt wire was taken as a counter electrode and Ag/AgCl ($E_{\text{Ag/AgCl}} = 0.197$) with saturated (3 M) KCl was used as a reference electrode under light illumination. The electrolyte used was 0.25M Na₂S/0.35M Na₂SO₃ aqueous solution (PH = 13.1). Linear sweep voltammetry was recorded under front side radiance against Ag/AgCl to get the J-V curve of the working electrode at a scan rate of 20 mV. The analysis was performed using a tungsten lamp with an irradiance of 100 mW/cm² without UV & Visible filter and voltage was between -0.7 V to 1 V.

The measured potential was converted into reversible hydrogen potential (RHE) vs. Ag/AgCl using the Nernst equation;

$$E_{\text{RHE}} = E_{\text{Ag/AgCl}} + 0.059 \cdot \text{pH} + E^{\circ}_{\text{Ag/AgCl}} \quad (1)$$

Here E_{RHE} shows the converted potential vs. RHE, $E_{\text{Ag/AgCl}}$ represent the experimental potential measured against the Ag/AgCl reference electrode, $E^{\circ}_{\text{Ag/AgCl}}$ is the standard potential of Ag/AgCl (0.197), and the pH of electrolyte (= 13.1) in this case[55].

Chronoamperometric (I-t) technique was performed at a potential of 0.3 V against Ag/AgCl reference electrode in the presence of light to check samples' stability. Electrochemical impedance spectroscopy (EIS) analysis was performed in light and dark in the frequency range from 0.2 Hz to 10^5 Hz with an AC potential amplitude of 10 mV under open circuit potential (OCP). Mott-Schottky analysis were carried out at 1 kHz frequency under a dark environment; -0.5 V to +0.0 V vs. Ag/AgCl electrode.

Chapter-04

Results & Discussion

Chapter-04

4. Results & Discussions:

4.1 XRD ANALYSIS:

To examine the structural properties of synthesized photoelectrocatalyst, the XRD analysis was performed as shown in Figure 1(a-e). The samples shown in Fig. 1(a-e) possess highly polycrystalline anatase TiO₂ phase (JCPDS 02-0406) with the diffraction peaks observed at $2\theta = 25.42^\circ, 37.98^\circ, 38.55^\circ, 53.24^\circ, 70.87^\circ,$ and 76.38° correspond to [101], [004], [112], [105], [220] and [301] planes respectively. The single large peak observed at 40.43° corresponds to [101] represent the background signal of Ti-foil figure 1(a-e). The two peaks observed at $2\theta = 47.81^\circ$ and 62.88° corresponds to [400] and [511] respectively which confirms the deposition and presence of CoFe₂S₄, Fig. 1 (d-e)[50].

Thus Fig. 1 (b-e) showed the suppression of various peak intensities with increasing loading of CoFe₂S₄/TiO₂ NTS. The reason could be the small crystallite size of CoFe₂S₄ or because of the minimum exposure of it to the x-rays due to its high dispersion inside the TiO₂ nanotubes[56-59]. A little shifting in XRD peaks was also observed as in-set (figure 1), which confirms that the material (CoFe₂S₄) and substrate (pristine TiO₂ NTs) have highly interacted.

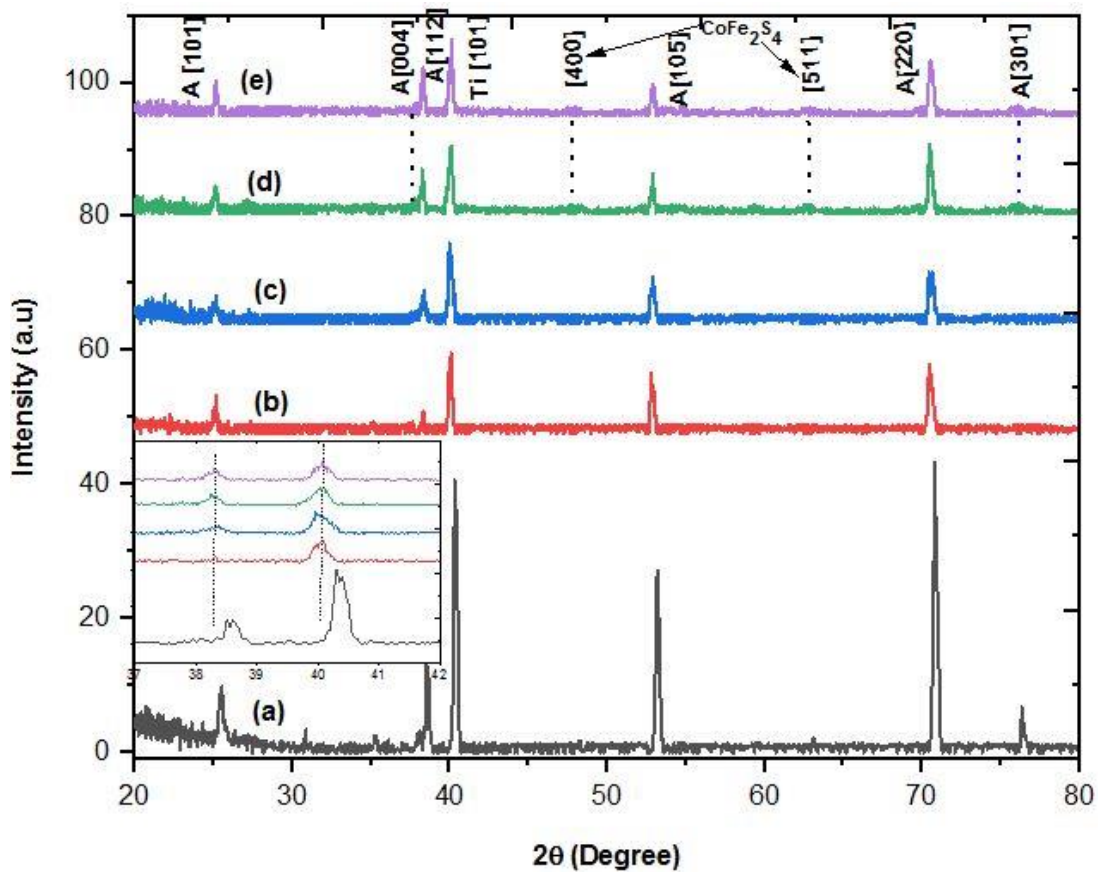


Figure 18 XRD patterns of (a) pristine TiO₂ NTs (b) 05 (c) 10 (d) 15 and (e) 20-CoFe₂S₄/TiO₂ NTs

4.2 SEM analysis along with Energy dispersive spectroscopy (EDS):

The SEM images shown in Fig. 2(a-d) gives us information about the sample structure, and surface morphology in a rough scale measurement. Herein, figure 2 represent the top view of the TiO₂ nanotubes with different loading cycles of CoFe₂S₄/TiO₂ NTs on Ti substrate shown in Fig. 2(a-d). Thus a smooth, clean surface with tube opening can easily be observed with tube diameter of 36.76 nm, while nanotubes' wall thickness was about 28.37 nm containing almost spherical particles of CoFe₂S₄ (figure 2(a-d)). All the samples exhibited well-developed nanotubes, with CoFe₂S₄ properly embedded in the case of 05-CoFe₂S₄/TiO₂ NTs, while it is deposited on pristine TiO₂ NTs surface in the case of 10-CoFe₂S₄/TiO₂ NTs and 15-CoFe₂S₄/TiO₂ NTs shown in Fig. 2(a-d) respectively.

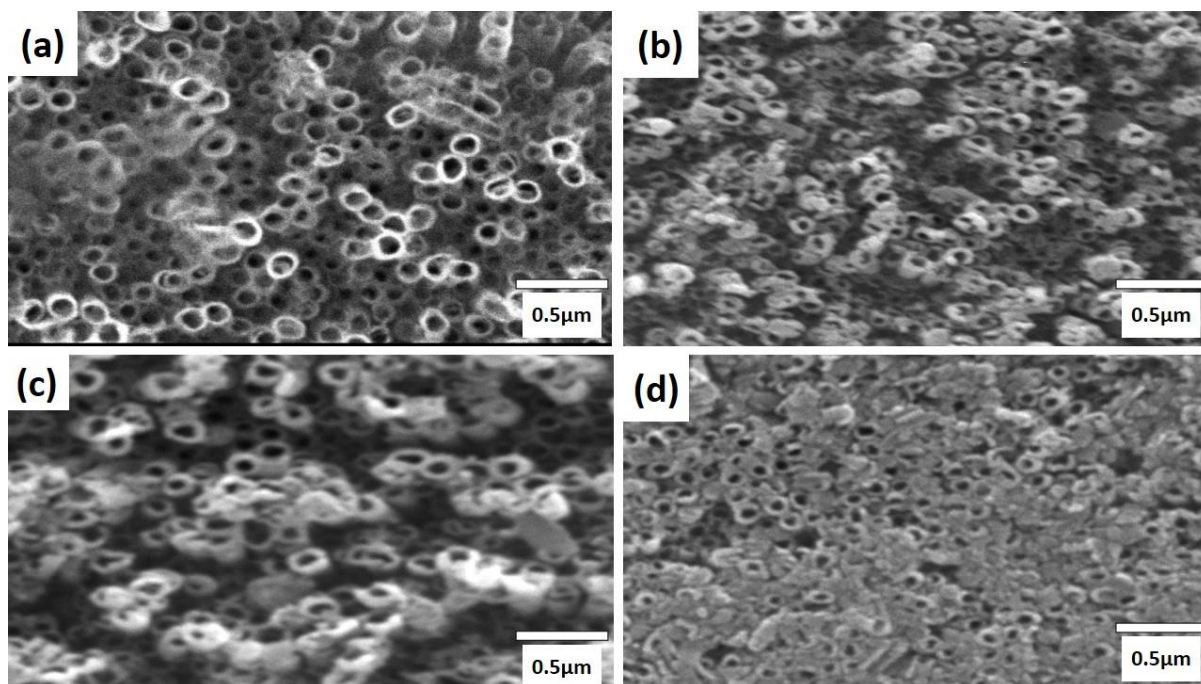


Figure 19 SEM images of (a) 05 (b) 10 (c) 15 (d) 20-CoFe₂S₄/TiO₂ NTs

The energy-dispersive X-ray spectroscopy (EDS) analysis was shown in figure 3(a,b), indicating the presence of Ti, O, Co, Fe, and S. The Figure 3(a,b) clearly shown that, Co, Fe and S were found with approximately 1:2:4 ratios respectively suggesting that CoFe₂S₄ synthesized successfully. Thus it confirmed the uniform distribution of CoFe₂S₄ over the TiO₂ NTs array or CoFe₂S₄ was embedded properly inside the tubes. Here Ti:O ratio was found to be 1:2 ratio which confirms that TiO₂ nanotubes (NTs) was successfully prepared shown in Fig. 3(a,b).

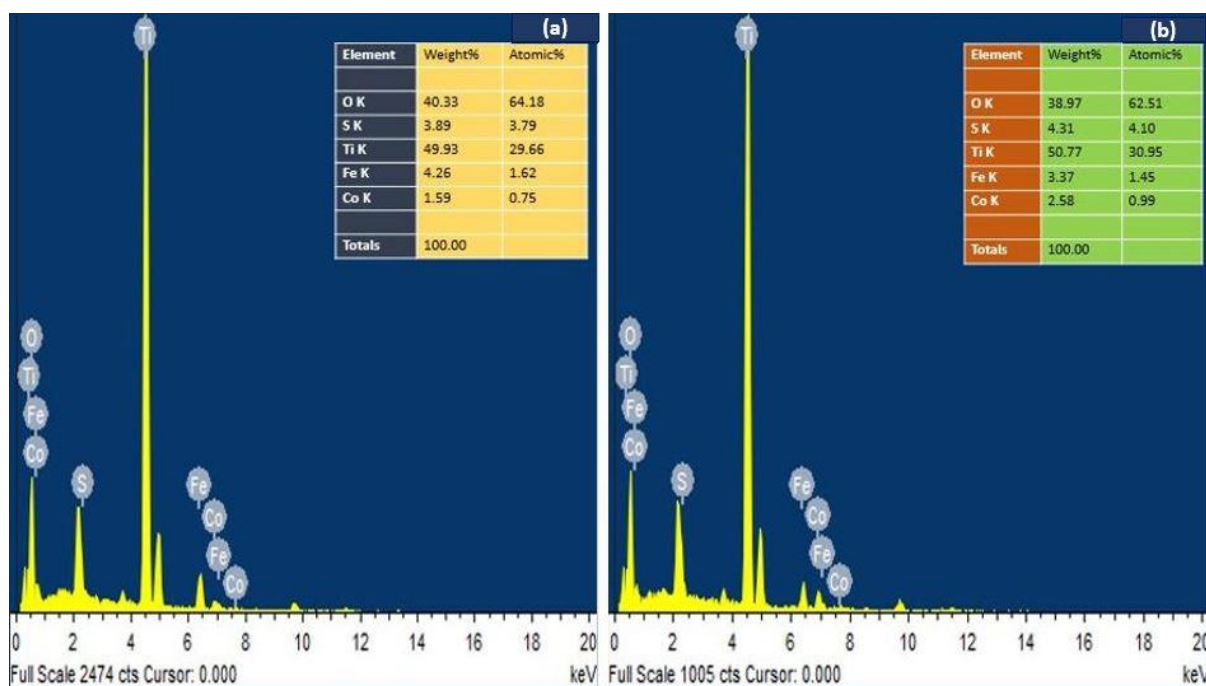


Figure 20 EDS spectrum of (a) 15 (b) 20-CoFe₂S₄/TiO₂ NTs

4.3 Raman Spectroscopy:

Raman analysis was performed to confirm the vibrational modes of photoelectrocatalyst as shown in figure 4(a-e). Herein, Fig. 4(a) TiO₂ nanotubes spectra exhibited active modes peaks at 148.5, 199.43, 397, 517.82, and 634.65 cm⁻¹ respectively, which corresponds to A_{1g} (517.82 cm⁻¹), 2B_{1g} (397 and 517.82 cm⁻¹) and 3E_g (148.5, 199.43 and 634.65 cm⁻¹) respectively. This confirms the formation of the pure anatase phase. While Raman peaks at 431 cm⁻¹ and 587cm⁻¹ results in spacing and large shifting occurs which confirms the presence of CoFe₂S₄ Fig. 22 (d-e). Since Raman spectra exhibit the presence of chemical and /or physical interaction between CoFe₂S₄ nanoparticles with pristine TiO₂ nanotubes, such effect can be assigned to changes of vibrational modes of anatase structure at the TiO₂ nanotubes by deposited CoFe₂S₄ nanoparticles. Fig. 4(b-e) shows a little shifting of peaks towards higher wavenumbers (shown in inset) which are credited to the oxygen vacancies in the surface due to interaction between CoFe₂S₄ and TiO₂ NTs. Ascribed to the generation of oxide (O⁻) vacancies, the lattice shrinks, thus peaks shift to higher wavenumber[60-63]. As loading of CoFe₂S₄ increases on TiO₂ NTs, the intensity of TiO₂ NTs peaks is increasing, illustrating the homogenous deposition and loading of CoFe₂S₄ at TiO₂ NTs. It is noticed as in Fig. 4(d-e) that 15-CoFe₂S₄/TiO₂ NTs and 20-CoFe₂S₄ shows high intensive peaks compared to pristine-TiO₂ NTs, 05-CoFe₂S₄/TiO₂

NTs, and 10-CoFe₂S₄/TiO₂ NTs, as CoFe₂S₄ nanoparticles were properly deposited inside as well as upon the surface of the titania nanotubes, which were shown clearly in the SEM images (Fig. 2(c-d)).

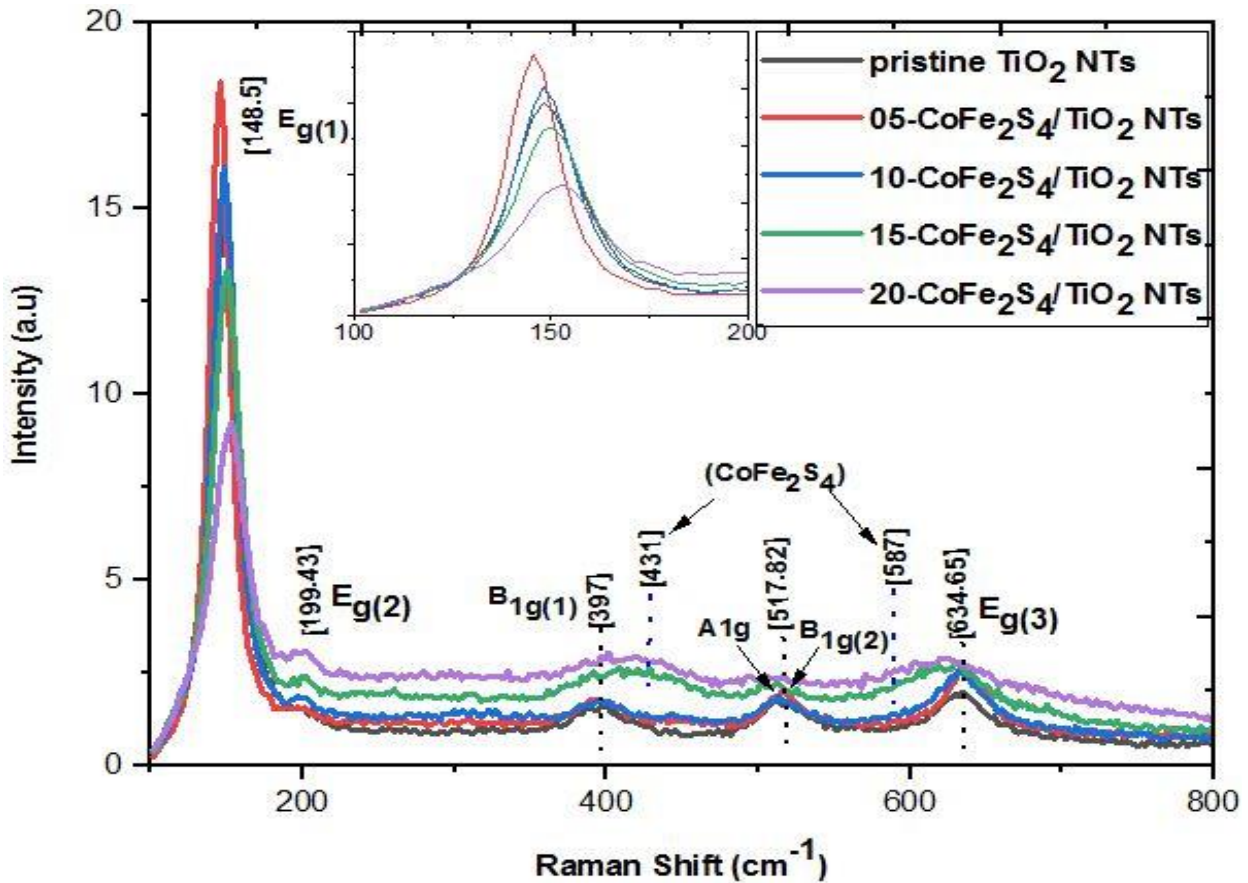


Figure 21 Raman Spectra of (a) Pristine TiO₂ NTs (b) 05 (c) 10 (d) 15 (e) 20-CoFe₂S₄/TiO₂ NTs

4.4 UV-Vis Diffuse Reflectance Spectroscopy:

The diffuse reflectance spectra of pristine TiO₂ NTs and CoFe₂S₄/TNT of 5, 10, 15 & 20 SILAR cycles are shown in Figure 5(a-b). A sharp decline in absorbance was noticed at around 397 nm for pristine TiO₂ nanotubes, which is caused by the electron transfer from valence band (VB) O_{2p} states to the conduction band of Ti^{3d} states, and the absorption peak is red shifted when TiO₂ nanotubes are decorated with CoFe₂S₄[60, 64, 65]

The bandgap of all the samples were determined through the Kubelka-Munk function;

$$(F(R)hv)^{1/2} = A(hv-E_g) \quad (2)$$

Here $F(R)$ is the Kubelka-Munk function, A is constant, ν is the radiation frequency, h is Planck constant and E_g is the bandgap energy[66]. From the figure 5(b) below, it is noted that CoFe_2S_4 powder and TiO_2 possesses a direct bandgap, which is found to be 2.27 eV for CoFe_2S_4 , 3.12 eV for pristine TiO_2 NTs, 3.07 eV for 05- $\text{CoFe}_2\text{S}_4/\text{TiO}_2$ NTs, 3.04 eV for 10- $\text{CoFe}_2\text{S}_4/\text{TiO}_2$ NTs, 2.92 eV for 15- $\text{CoFe}_2\text{S}_4/\text{TiO}_2$ NTs and 2.99 eV for 20- $\text{CoFe}_2\text{S}_4/\text{TiO}_2$ NTs respectively. This shows that the bandgap decreases first for moderate deposition of CoFe_2S_4 , while it again increases after maximum amount of loading of CoFe_2S_4 over TiO_2 NTs.

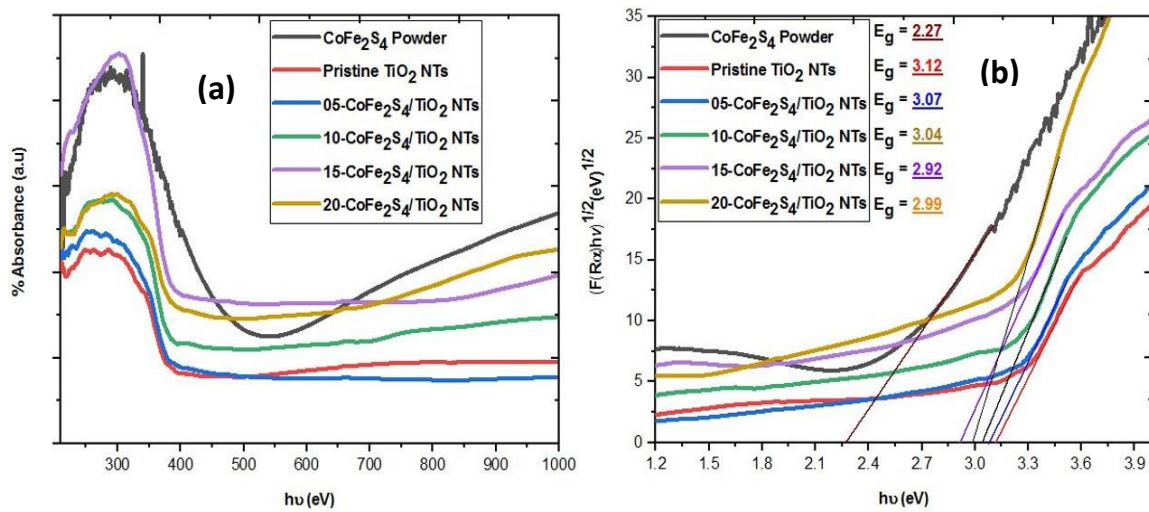


Figure 22 (a) UV-Vis & (b) DRS spectra of CoFe_2S_4 powder, pristine TiO_2 NTs, 05, 10, 15, 20- $\text{CoFe}_2\text{S}_4/\text{TiO}_2$ NTs

4.5 Fourier Transform Infrared Spectroscopy (FTIR):

Different peaks of pristine TiO_2 NTs and $\text{CoFe}_2\text{S}_4/\text{TiO}_2$ NTs having various SILAR cycles were analyzed in the wavelength range of $4000\text{-}500\text{cm}^{-1}$ shown in Fig. 6(a). Broadband was observed within $3000\text{-}3500\text{ cm}^{-1}$, which has been assigned to the hydroxyl group (OH) stretching vibration of the TiO_2 surface. The bands at around $1500\text{-}1600\text{ cm}^{-1}$ have been assigned to the (O-H) bending vibration of water or Ti-OH, showing the adsorbed water molecules[67]. The bands obtained at 650 and 1400 cm^{-1} referred to the lattice vibration of the Ti-O-Ti stretching mode[68]. While Ti-O-O characteristics vibration peaks were assigned to the range of $900\text{-}600\text{ cm}^{-1}$. A slight shifting of peaks was also recorded due to CoFe_2S_4 accumulation at around $500\text{-}700\text{ cm}^{-1}$, indicating the asymmetrical vibration of Ti-Fe-O.

4.6 Fluorescence Spectroscopy (FL):

Fluorescence (FL) emission spectra are mainly related to transfer, photocatalytic activity, and photogenerated electron-hole (e^-/h^+) pairs recombination in the semiconductor. The excitation wavelength of 400 nm was applied to get the FL spectra shown in Fig. 6(b). Herein pristine TiO_2 NTs shows a stronger intensity than 05- $\text{CoFe}_2\text{S}_4/\text{TiO}_2$ NTS, 10- $\text{CoFe}_2\text{S}_4/\text{TiO}_2$ NTS, 15- $\text{CoFe}_2\text{S}_4/\text{TiO}_2$ NTS, and 20- $\text{CoFe}_2\text{S}_4/\text{TiO}_2$ NTS suggesting that the recombination of photogenerated (e^-/h^+) pairs are higher in pure TiO_2 NTs, with very lower photocatalytic activity than 05- $\text{CoFe}_2\text{S}_4/\text{TiO}_2$ NTS, 10- $\text{CoFe}_2\text{S}_4/\text{TiO}_2$ NTS, 15- $\text{CoFe}_2\text{S}_4/\text{TiO}_2$ NTS and 20- $\text{CoFe}_2\text{S}_4/\text{TiO}_2$ NTS respectively. The 15- $\text{CoFe}_2\text{S}_4/\text{TiO}_2$ possesses better photocatalytic activity and having very lower (e^-/h^+) pairs recombination properties.

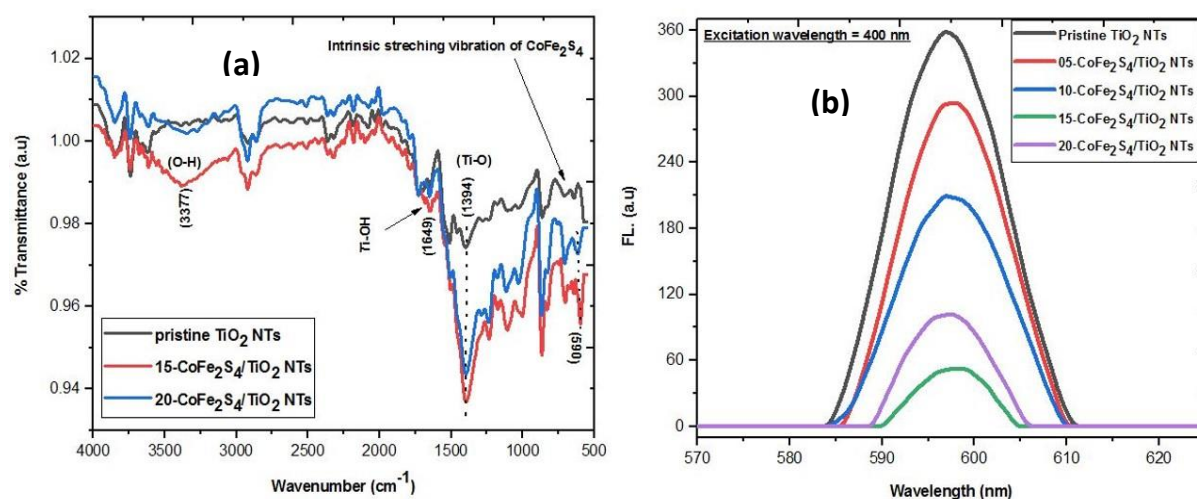


Figure 23 (a) FTIR spectra pristine TiO_2 NTs, 15 and 20- $\text{CoFe}_2\text{S}_4/\text{TiO}_2$ NTS (b) FL spectra of Pristine TiO_2 NTs and $\text{CoFe}_2\text{S}_4/\text{TiO}_2$ NTS (05, 10, 15 and 20 cycles)

4.7 Photoelectrochemical Analysis (PEC):

A photoelectrochemical (PEC) water splitting of pristine and modified TiO_2 nanotubes was recorded under illumination using 0.25M Na_2S and 0.35M Na_2SO_3 (PH = 13.1) as an electrolyte, where the photocurrent densities varied by changing the amount of CoFe_2S_4 . It is noted that Na_2S and Na_2SO_3 possess lower energy consumption and easy oxidizability property, thus considered as a suitable electrolytes in this case. Reactions occur during photocatalytic water splitting in the presence of Na_2S and Na_2SO_3 [69]. Electrons in semiconductors can only be excited to their conduction band (CB) by light absorption with

energy greater than their bandgap, leaving behind electron deficiencies i.e holes in the valence band (VB). The photoexcited electrons get absorbed by water molecules from the CB of the catalyst to form H₂ gas. Simultaneously; holes (h⁺) present in the valence band oxidize SO₃²⁻ to SO₄²⁻ and S₂²⁻. A resultant colorless compound, S₂O₃²⁻ thus generated due to the mutual coupling of S₂²⁻ and SO₃²⁻. While in the last excess of S²⁻ ion is scavenged by SO₃²⁻ shown in Fig. 9(d).

The present study revealed that sulfide oxidation (Na₂S aqueous electrolyte) happens to be the dominant anodic reaction for photocurrent generation and charge transfer. Na₂SO₃ acts as a reducing agent that causes the regeneration of the S⁻² ion in the electrolyte and thus enhances the rate of oxidation which in turn sustains the molecular hydrogen evolution occurring at the cathode. Otherwise, it would be diminished with time due to disulfide, S₂²⁻ formation. To conclude, the sulfide ions behave as a sacrificial chemical species generating fast kinetics electrons. These electrons reaches the cathode to assist molecular hydrogen production.

The photoelectrochemical performance of the photocatalyst was examined and linear sweep voltammograms were recorded under illumination of light shown in Fig 8(a). Pristine TiO₂ NTs, 05-CoFe₂S₄/TiO₂ NTs, 10-CoFe₂S₄/TiO₂ NTs, 15-CoFe₂S₄/TiO₂ NTs and 20-CoFe₂S₄/TiO₂ NTs showed a photocurrent density (J) of 0.78, 1.04, 1.75, 2.95 and 2.30 mAcm⁻² respectively at 0.26 V against Ag/AgCl (1.23 V vs. RHE) illuminated by tungsten lamp with input power of 100 mW/cm² without UV-Vis light filter. Figure 8(a) shows a gradual increase in current density up to 15-CoFe₂S₄/TiO₂ NTs with moderate deposition of CoFe₂S₄, which starts decreasing as the deposition exceeds its limit. Figure 8(a) for J-V character, shows the gradual rise in the photocurrent response forming a bump for 15-CoFe₂S₄/TiO₂ NTs and 20-CoFe₂S₄/TiO₂ NTs photocatalyst at around 0.73 V vs. RHE because the photogenerated charges have excited from valence band (VB) to the conduction band (CB) until a point of saturation is thus acquired, as majority photoexcited electrons occupy the CB thus, fulfilling the active site on the photocatalyst surface[70]. The photoelectrochemical activity of 15-CoFe₂S₄/TiO₂ NTs were compared with different photoanodes in literature as given in table 2.

Table 2 Comparison with references

Sample composition	Method of synthesis	Electrolyte used	Light source	Current density	References
				J (mAcm⁻²)	
(Co/S-gC ₃ N ₄ /BiOCl)	Ultrasonic assisted hydrothermal method	0.5 M Na ₂ SO ₃ + NaHCO ₃	Light illumination with AM 1.5G	0.393	[71]
CoO _x /BiVO ₄	Impregnation and calcination method	0.5 M Na ₂ SO ₄	Xenon lamp with AM 1.5G	3.1	[72]
ZnO/CoO/core/shell	ALD, CBD and electrochemical deposition	30 mM Borax with NaOH	Ozone free Xenon lamp (300 W)	1.25	[73]
BiVO ₄ /NiCo-layered double hydroxide (LDH)	Semiconductor modification with cocatalyst	Na ₂ SO ₄ of 0.5M	Xenon lamp (AM 1.5G) with monochromator	3.4	[74]
15-CoFe ₂ S ₄ /TiO ₂ NTs	Anodization, SILAR & CVD	0.25 M Na ₂ S + 0.35 M Na ₂ SO ₃	Tungsten lamp	2.95	<i>This work</i>

The percentage solar to hydrogen efficiency (%STH) was determined for photoanode using the formula;

$$\% \eta = I(1.23 - V) / P_{in} \times 100 \quad (3)$$

In the above equation, I represent the photocurrent density at any calculated potential, η shows %STH, V shows the given potential against RHE, P_{in} is the incident light intensity at 100 mW/cm²[75]. Pristine TiO₂ NTS, 05-CoFe₂S₄/TiO₂ NTs, 10-CoFe₂S₄/TiO₂ NTs, 15-CoFe₂S₄/TiO₂ NTs and 20-CoFe₂S₄/TiO₂ NTs exhibit a %STH efficiency of 0.43 %, 0.45 %, 0.85 %, 1.42 % and 0.95 % at an applied potential of 0.56, 0.61, 0.63, 0.62 and 0.60 V (vs.

RHE) respectively. The maximum %STH efficiency was obtained by 15-CoFe₂S₄/TiO₂ NTs versus 0.69 V (vs. RHE). These results matched fully with the *J-V* characteristics.

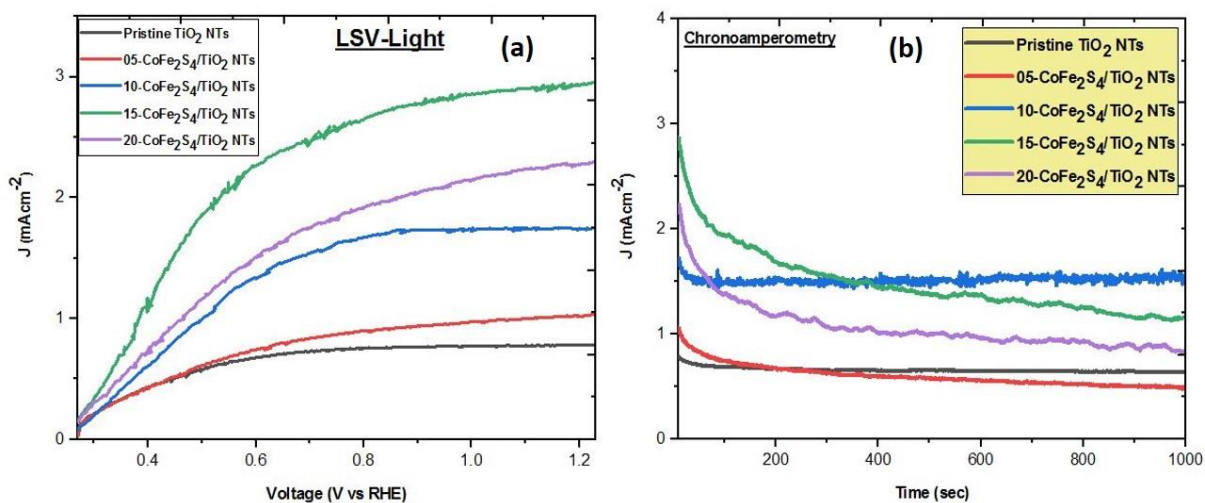


Figure 24 (a) LSV (*J-V*) curves & (b) Chronoamperometry (*I-t*) curves of TiO₂ NTs, 05, 10, 15, and 20-CoFe₂S₄/TiO₂ NTs

To check the stability and further activity of the electrodes, chronoamperometry was performed shown in figure 8 (b). The potential used was in between the range of 0 to 0.5 V for the activity. There was an initial sharp current drop from 2.89 mAcm⁻² at 06 sec to 2.04 mAcm⁻² at 65 sec and to 1.46 mAcm⁻² at 380 sec and then get stable after that, thus high current densities are shown by 15-CoFe₂S₄/TiO₂ NTs. While a drop in current for 20-CoFe₂S₄/TiO₂ NTs due to high deposition of CoFe₂S₄ occurs from 2.26 mAcm⁻² at 06 sec, to 1.06 mAcm⁻² at 173 sec and keeps on decreasing, showing that surface poisoning or changes in the structure of electrodes might occur[76]. No such changes were noticed for pristine TiO₂ NTs, 05-CoFe₂S₄/TiO₂ NTs and 10-CoFe₂S₄/TiO₂ NTs respectively which show better stability due to little amount of CoFe₂S₄ loading over TiO₂ NTs.

Mott-Schottky analysis ($1/C^2$ vs. potential) was performed to find out the flat band potential (E_{fb}) at a fixed frequency of 1000 Hz in 0.25 M Na₂S and 0.35 M Na₂SO₃ aqueous electrolyte solution. E_{fb} was determined by extrapolating a tangential line from the linear plot of $1/C^2$ vs. E shown in figure 9(a)[77]. The value of E_{fb} was found to be 0.12, 0.25, 0.18, 0.09 and 0.13 V vs. RHE for pristine TiO₂ NTs, 05-CoFe₂S₄/TiO₂ NTs, 10-CoFe₂S₄/TiO₂ NTs, 15-CoFe₂S₄/TiO₂ NTs and 20-CoFe₂S₄/TiO₂ NTs respectively. The positive slope in figure 9(a) shows the n-type nature of the electrodes and thus shows better PEC activity which implies that CoFe₂S₄ deposition could not change the semiconductor type and thus CoFe₂S₄ deposited

TiO₂ NTs still exhibited n-type semiconductor nature. Additionally, the carrier's concentration can be approximated from the slope of respective plots using Eq. 4 below. Here, N_A and N_D represent the concentration of the acceptors & the donor carriers respectively[78].

$$N_D = (2/e_0\epsilon\epsilon_0)/[dC_s^2/dV]^{-1} \quad (4)$$

Where N_D represents the charge carrier density (donor density), e₀ is the charge on the electron, ε corresponds to the dielectric constant of sample and ε₀ indicates the permittivity of free space respectively. The values of N_D obtained from the slope of the graph was 1.14×10⁻²², 1.11×10⁻²², 1.56×10⁻²², and 2.64×10⁻²³ cm⁻³ for 05, 10, 15 and 20-CoFe₂S₄/TiO₂ NTs respectively as recorded in table 3. The increased donor density demonstrates minimum charge recombination and visible light absorption in CoFe₂S₄/TiO₂ NTs (various cycles). Thus 15-CoFe₂S₄/TiO₂ NTs demonstrated better PEC water splitting performance than others due to the high value of charge carrier density.

Table 3 Summary of photoelectrochemical data

Sample composition	Current Density	Difference	Current sensitivity	Mid Frequency at minimum phase	Electron life time	Flat band potential	Band gap	Donor Density
	<i>J (Light)</i>	<i>IL-ID</i>	<i>IL/ID</i>	<i>f_{min}</i>	<i>τ_e</i>	<i>V_{FB}</i>	<i>E_g</i>	<i>N_D</i>
	<i>mAc^{m-2}</i>	<i>mAc^{m-2}</i>		<i>Hz</i>	<i>μs</i>	<i>V</i>	<i>eV</i>	<i>cm⁻³</i>
	(at 1.23 V)		(at 1.23 V)	Light	Light		CoFe ₂ S ₄ = 2.27	
Pristine TiO ₂ NTs	0.78	0.1	1.15	475.02	335.22	0.12	3.12
05-CoFe ₂ S ₄ /TiO ₂ NTs	1.04	0.2	1.24	141.13	1128.29	0.25	3.07	1.14×10 ⁻²²
10-CoFe ₂ S ₄ /TiO ₂ NTs	1.75	0.86	1.96	120.67	1319.61	0.18	3.04	1.11×10 ⁻²²
15-CoFe₂S₄/TiO₂ NTs	2.95	1.91	2.84	1.10	144759.7	0.09	2.92	1.56×10⁻²²
20-CoFe ₂ S ₄ /TiO ₂ NTs	2.30	1.38	2.50	9.85	16166.06	0.13	2.99	0.264×10 ⁻²²

The EIS studies were done to determine the charge transfer resistance (R_{ct}) at the junction between photoanode and electrolyte solution[79]. The respective Nyquist plots achieved for pristine TiO_2 NTs, 05, 10, 15 and 20- $CoFe_2S_4/TiO_2$ NTs using UV-visible light irradiation are presented in figure 9(b) to understand in-depth charge recombination, separation, and its transportation at the interface between photoelectrode-electrolyte. All of the samples appeared a semi-circle. An arc of a smaller radius reveals a smaller charge transfer resistance (R_{ct}) with an efficient charge transfer from semiconductor to electrolyte[80]. The circle radius for 15- $CoFe_2S_4/TiO_2$ NTs was little more compared to pristine TiO_2 NTs, showing that recombination decreases significantly much more in $CoFe_2S_4/TiO_2$ NTs heterostructure as shown by LSV and FL results, depicting better charge transfer in 15- $CoFe_2S_4/TiO_2$ NTs, as compared to pristine TiO_2 NTs while overloading in 20- $CoFe_2S_4/TiO_2$ NTs results in higher charge transfer resistance R_{ct} .

The bode plot between phase angle and frequency were shown in figure 9(c), indicated that the mid-frequency at minimum phase angle is shifted towards lower frequency with increasing doping growth under illumination, where the photoexcited electrons lifetime was measured by $\tau = 1/2\pi f_{mid}$ using mid-frequency at minimum phase angle (f_{mid}) of the bode plot as given in table 2[66]. Quantitatively, the lifespan of the charge carriers in pristine TiO_2 NTs, 05- $CoFe_2S_4/TiO_2$ NTs, 10- $CoFe_2S_4/TiO_2$ NTs, 15- $CoFe_2S_4/TiO_2$ and 20- $CoFe_2S_4/TiO_2$ NTs was calculated to be 335.22 μs , 1128.29 μs , 1319.61 μs , 144759.7 μs and 16166.06 μs respectively. The lifetime of the electrons is inversely related to the mid-frequency at minimum phase angle while it is directly proportional to the charge transfer resistance (R_{ct}). Thus it is observed that 15- $CoFe_2S_4/TiO_2$ NTs possess higher lifetime of electron and are stable for longer time when generated.

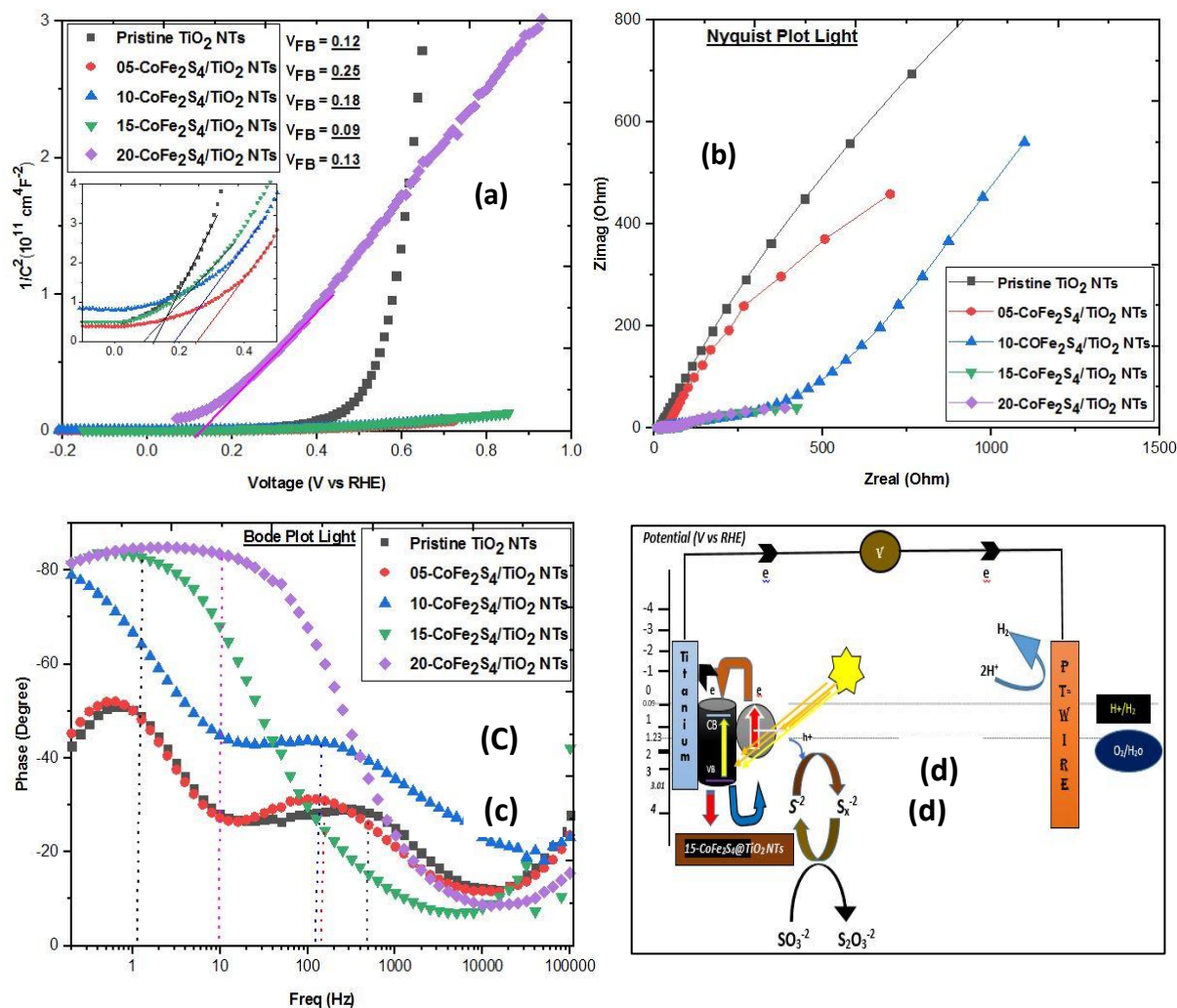


Figure 25 (a) Mott-Schottky plots of the samples (b) Nyquist plot of the photoanode (c) Bode plot of samples under light (d) Proposed mechanism of photoelectrocatalysts.

4.8 Conclusion:

We demonstrated that CoFe₂S₄/TiO₂ arrays manufactured by simple electrochemical anodization, followed by the SILAR technique and its treatment under S atmosphere using CVD process respectively have improved PEC behavior in comparison with pristine TiO₂ nanotubes. It was noticed that 15-CoFe₂S₄/TiO₂ NTs showed better photoelectrochemical properties, with superior charge carrier density (N_D) of $1.56 \times 10^{-22} \text{ cm}^{-3}$ and have lower electron-hole (e^-/h^+) pair recombination but lower stability because of high loading of CoFe₂S₄ over TiO₂ NTs. A high stability were observed for 10-CoFe₂S₄/TiO₂ NTs, due to intermediate loading of CoFe₂S₄ over TiO₂ NTs having optimum thickness. A uniform distribution of CoFe₂S₄ on TiO₂ nanotubes was confirmed by EDS, XRD confirmed its crystalline phase, while FL and EIS illustrated the effective interchange of charge between TiO₂ nanotubes and

CoFe₂S₄ interfaces. A higher photocurrent density of 2.95 mAcm⁻² was recorded for 15-CoFe₂S₄/TiO₂ NTs, with current sensitivity is 2.46 times higher than pristine TiO₂ NTs. 10-CoFe₂S₄ show higher stability compared to 15-CoFe₂S₄/TiO₂ and 20-CoFe₂S₄/TiO₂ NTs respectively. Finally, it's worthy to highlight that the presented research here is facile, low-cost, easy to synthesize the nanocomposite, and could pave the way to develop new semiconductor nanocomposite based on TiO₂ nanotube with high PEC water splitting.

Chapter-05
References

5. References:

- [1] A. Ahmadi, J. Beheshtian, N.L.J.P.E.L.-d.S. Hadipour, Nanostructures, Interaction of NH₃ with aluminum nitride nanotube: electrostatic vs. covalent, 43 (2011) 1717-1719.
- [2] J. Beheshtian, M.T. Baei, A.A. Peyghan, Z.J.J.o.m.m. Bagheri, Electronic sensor for sulfide dioxide based on AlN nanotubes: a computational study, 18 (2012) 4745-4750.
- [3] L. Pauling, R.J.A.S.U.A. Corey, Proc. nat, 16 (1930) 578.
- [4] T.F. Bates, L.B. Sand, J.F.J.S. Mink, Tubular crystals of chrysotile asbestos, 111 (1950) 512-513.
- [5] P. Cradwick, V. Farmer, J. Russell, C. Masson, K. Wada, N.J.N.P.S. Yoshinaga, Imogolite, a hydrated aluminium silicate of tubular structure, 240 (1972) 187-189.
- [6] C. Ye, G. Meng, Z. Jiang, Y. Wang, G. Wang, L.J.J.o.t.A.C.S. Zhang, Rational growth of Bi₂S₃ nanotubes from quasi-two-dimensional precursors, 124 (2002) 15180-15181.
- [7] R.J.C. Tenne, S.A. Physicochemical, E. Aspects, Fullerene-like materials and nanotubes from inorganic compounds with a layered (2-D) structure, 208 (2002) 83-92.
- [8] A. Zak, L.S. Ecker, R. Efrati, L. Drangai, N. Fleischer, R.J.S. Tenne, Transducers, Large-scale Synthesis of WS₂ Multiwall Nanotubes and their Dispersion, an Update, 12 (2011) 1.
- [9] G. Radovsky, R. Popovitz-Biro, M. Staiger, K. Gartsman, C. Thomsen, T. Lorenz, G. Seifert, R.J.A.C. Tenne, Synthesis of copious amounts of SnS₂ and SnS₂/SnS nanotubes with ordered superstructures, 123 (2011) 12524-12528.
- [10] I.D. Muhammad, M. Awang, O.B. Mamat, Z. Lockman, Review of the Geometric Dimensions of Cubic Zirconia Nanotubes, A paper presented at the 3rd international conference on plant equipment and reliability (ICPER 2012), KLCC Convention Centre, Kuala Lumpur, 2012, pp. 12-14.
- [11] S.-I. Na, S.-S. Kim, W.-K. Hong, J.-W. Park, J. Jo, Y.-C. Nah, T. Lee, D.-Y.J.E.A. Kim, Fabrication of TiO₂ nanotubes by using electrodeposited ZnO nanorod template and their application to hybrid solar cells, 53 (2008) 2560-2566.
- [12] M. Krause, A. Mücklich, A. Zak, G. Seifert, S.J.p.s.s. Gemming, High resolution TEM study of WS₂ nanotubes, 248 (2011) 2716-2719.
- [13] Y.Q. Zhu, T. Sekine, K.S. Brigatti, S. Firth, R. Tenne, R. Rosentsveig, H.W. Kroto, D.R.J.J.o.t.A.C.S. Walton, Shock-wave resistance of WS₂ nanotubes, 125 (2003) 1329-1333.
- [14] C.S. Reddy, A. Zak, E.J.J.o.M.C. Zussman, WS₂ nanotubes embedded in PMMA nanofibers as energy absorptive material, 21 (2011) 16086-16093.
- [15] R. Kreizman, A.N. Enyashin, F.L. Deepak, A. Albu-Yaron, R. Popovitz-Biro, G. Seifert, R.J.A.F.M. Tenne, Synthesis of core-shell inorganic nanotubes, 20 (2010) 2459-2468.
- [16] G. Lalwani, A.M. Henslee, B. Farshid, P. Parmar, L. Lin, Y.-X. Qin, F.K. Kasper, A.G. Mikos, B.J.A.b. Sitharaman, Tungsten disulfide nanotubes reinforced biodegradable polymers for bone tissue engineering, 9 (2013) 8365-8373.
- [17] Z.N. Jameel, A.J. Haider, S.Y. Taha, S. Gangopadhyay, S. Bok, Evaluation of hybrid sol-gel incorporated with nanoparticles as nano paint, AIP Conference Proceedings, AIP Publishing LLC, 2016, pp. 020001.
- [18] A.J. Haider, Z.N. Jameel, I.H.J.E.P. Al-Hussaini, Review on: titanium dioxide applications, 157 (2019) 17-29.
- [19] B. O'regan, M.J.n. Grätzel, A low-cost, high-efficiency solar cell based on dye-sensitized colloidal TiO₂ films, 353 (1991) 737-740.
- [20] D.A. Hanaor, C.C.J.A.E.M. Sorrell, Sand Supported Mixed-P hase Ti O₂ Photocatalysts for Water Decontamination Applications, 16 (2014) 248-254.
- [21] T. Hirakawa, K. Yawata, Y.J.A.C.A.G. Nosaka, Photocatalytic reactivity for O₂- and OH radical formation in anatase and rutile TiO₂ suspension as the effect of H₂O₂ addition, 325 (2007) 105-111.
- [22] Z. Huang, P.-C. Maness, D.M. Blake, E.J. Wolfrum, S.L. Smolinski, W.A.J.J.o.P. Jacoby, P.A. Chemistry, Bactericidal mode of titanium dioxide photocatalysis, 130 (2000) 163-170.
- [23] S. Sreekantan, L.C. Wei, Z.J.J.o.t.E.S. Lockman, Extremely fast growth rate of TiO₂ nanotube arrays in electrochemical bath containing H₂O₂, 158 (2011) C397.

- [24] G.K. Mor, O.K. Varghese, M. Paulose, C.A.J.A.F.M. Grimes, Transparent highly ordered TiO₂ nanotube arrays via anodization of titanium thin films, 15 (2005) 1291-1296.
- [25] J.H. Jung, T. Shimizu, S.J.J.o.M.C. Shinkai, Self-assembling structures of steroidal derivatives in organic solvents and their sol-gel transcription into double-walled transition-metal oxide nanotubes, 15 (2005) 3979-3986.
- [26] Q. Ji, R. Iwaura, T.J.C.o.M. Shimizu, Regulation of silica nanotube diameters: sol-gel transcription using solvent-sensitive morphological change of peptidic lipid nanotubes as templates, 19 (2007) 1329-1334.
- [27] T.-S. Kang, A.P. Smith, B.E. Taylor, M.F.J.N.I. Durstock, Fabrication of highly-ordered TiO₂ nanotube arrays and their use in dye-sensitized solar cells, 9 (2009) 601-606.
- [28] M. Yoshimura, K.J.J.o.M.S. Byrappa, Hydrothermal processing of materials: past, present and future, 43 (2008) 2085-2103.
- [29] C.A.J.J.o.M.C. Grimes, Synthesis and application of highly ordered arrays of TiO₂ nanotubes, 17 (2007) 1451-1457.
- [30] M. Paulose, H.E. Prakasam, O.K. Varghese, L. Peng, K.C. Popat, G.K. Mor, T.A. Desai, C.A.J.T.J.o.P.C.C. Grimes, TiO₂ nanotube arrays of 1000 μm length by anodization of titanium foil: phenol red diffusion, 111 (2007) 14992-14997.
- [31] G.K. Mor, O.K. Varghese, M. Paulose, K. Shankar, C.A.J.S.E.M. Grimes, S. Cells, A review on highly ordered, vertically oriented TiO₂ nanotube arrays: Fabrication, material properties, and solar energy applications, 90 (2006) 2011-2075.
- [32] A.J.I.J.o.E. Pozio, Effect of Low cobalt loading on TiO₂ nanotube arrays for water-splitting, 2014 (2014).
- [33] J.M. Macak, P.J.E.A. Schmuki, Anodic growth of self-organized anodic TiO₂ nanotubes in viscous electrolytes, 52 (2006) 1258-1264.
- [34] J. Macak, H. Hildebrand, U. Marten-Jahns, P.J.J.o.E.C. Schmuki, Mechanistic aspects and growth of large diameter self-organized TiO₂ nanotubes, 621 (2008) 254-266.
- [35] N.K.A. Abdel-Motalib, An investigation into the doping and crystallinity of anodically fabricated titania nanotube arrays: Towards an efficient material for solar energy applications, The Pennsylvania State University 2009.
- [36] C. Ros, T. Andreu, J.R.J.J.o.M.C.A. Morante, Photoelectrochemical water splitting: a road from stable metal oxides to protected thin film solar cells, 8 (2020) 10625-10669.
- [37] C.-J. Lin, Y.-H. Yu, S.-Y. Chen, Y.-H.J.W.A.S.E.T. Liou, Anodic growth of highly ordered titanium oxide nanotube arrays: Effects of critical anodization factors on their photocatalytic activity, 65 (2010) 1094-1099.
- [38] B. Yao, Y. Chan, X.Y. Zhang, W. Zhang, Z. Yang, N.J.A.p.I. Wang, Formation mechanism of TiO₂ nanotubes, 82 (2003) 281-283.
- [39] M. Rahman, M. Hossain, B.J.M.E.R.J. Das, Synthesis of TiO₂ nanotube by electrochemical anodization of Ti foil in room temperature, 10 (2016) 90-93.
- [40] Z.R. Hesabi, N.K. Allam, K. Dahmen, H. Garmestani, M.A.J.A.a.m. El-Sayed, interfaces, Self-standing crystalline TiO₂ nanotubes/CNTs heterojunction membrane: Synthesis and characterization, 3 (2011) 952-955.
- [41] Z.-Y. Juang, C.-Y. Wu, A.-Y. Lu, C.-Y. Su, K.-C. Leou, F.-R. Chen, C.-H.J.C. Tsai, Graphene synthesis by chemical vapor deposition and transfer by a roll-to-roll process, 48 (2010) 3169-3174.
- [42] H. Zhao, H. Li, H. Chang, X. Quan, S.J.P. Chen, Fabrication and energetic performance in water treatment CNTs-TiO₂/Al₂O₃ composite membrane with a photocatalytic function, 14 (2014) 24-32.
- [43] M. Misra, K. Paramguru, S.J.J.o.n. Mohapatra, nanotechnology, Growth of carbon nanotubes on nanoporous titania templates, 7 (2007) 2640-2646.
- [44] A. Ali, W.-C.J.J.o.t.K.C.S. Oh, Photocatalytic performance of CoS₂-graphene-TiO₂ ternary composites for reactive black B (RBB) degradation, 54 (2017) 308-313.
- [45] A.A. Christy, D. Velauthapillai, CoS₂/TiO₂ Nanocomposites for Hydrogen Production under UV Irradiation, (2019).

- [46] S.W. Shin, J.Y. Lee, K.-S. Ahn, S.H. Kang, J.H.J.T.J.o.P.C.C. Kim, Visible light absorbing TiO₂ nanotube arrays by sulfur treatment for photoelectrochemical water splitting, 119 (2015) 13375-13383.
- [47] D.-Y. Wang, C.-H. Li, S.-S. Li, T.-R. Kuo, C.-M. Tsai, T.-R. Chen, Y.-C. Wang, C.-W. Chen, C.-C.J.S.r. Chen, Iron pyrite/titanium dioxide photoanode for extended near infrared light harvesting in a photoelectrochemical cell, 6 (2016) 1-7.
- [48] Y. Xin, Z. Li, W. Wu, B. Fu, Z.J.A.S.C. Zhang, Engineering, Pyrite FeS₂ sensitized TiO₂ nanotube photoanode for boosting near-infrared light photoelectrochemical water splitting, 4 (2016) 6659-6667.
- [49] I. Khan, A.J.A.S.C. Qurashi, Engineering, Sonochemical-assisted in situ electrochemical synthesis of Ag/ α -Fe₂O₃/TiO₂ nanoarrays to harness energy from photoelectrochemical water splitting, 6 (2018) 11235-11245.
- [50] K. Song, X. Chen, R. Yang, B. Zhang, X. Wang, P. Liu, J.J.C.E.J. Wang, Novel hierarchical CoFe₂Se₄@CoFe₂O₄ and CoFe₂S₄@CoFe₂O₄ core-shell nanoboxes electrode for high-performance electrochemical energy storage, 390 (2020) 124175.
- [51] X. Wang, Z. Li, Y. Zhang, Q. Li, H. Du, F. Liu, X. Zhang, H. Mu, J.J.C.E.J. Duan, Enhanced photocatalytic antibacterial and degradation performance by pnp type CoFe₂O₄/CoFe₂S₄/MgBi₂O₆ photocatalyst under visible light irradiation, 429 (2022) 132270.
- [52] P. Kulkarni, S. Nataraj, R.G. Balakrishna, D. Nagaraju, M.J.J.o.M.C.A. Reddy, Nanostructured binary and ternary metal sulfides: synthesis methods and their application in energy conversion and storage devices, 5 (2017) 22040-22094.
- [53] L. Huang, H. Wu, H. Liu, Y.J.E.A. Zhang, Phosphorous doped cobalt-iron sulfide/carbon nanotube as active and robust electrocatalysts for water splitting, 318 (2019) 892-900.
- [54] M. Gao, K. Le, W. Du, Z. Wang, F. Wang, W. Liu, J.J.N.J.o.C. Liu, Enhanced supercapacitive performance of the CoFe₂O₄/CoFe₂S₄ composite nanoflake array induced by surface sulfidation, 43 (2019) 13491-13498.
- [55] S. Hernández, D. Hidalgo, A. Sacco, A. Chiodoni, A. Lamberti, V. Cauda, E. Tresso, G.J.P.C.C.P. Saracco, Comparison of photocatalytic and transport properties of TiO₂ and ZnO nanostructures for solar-driven water splitting, 17 (2015) 7775-7786.
- [56] Z. Hua, Z. Dai, X. Bai, Z. Ye, P. Wang, H. Gu, X.J.C.E.J. Huang, Copper nanoparticles sensitized TiO₂ nanotube arrays electrode with enhanced photoelectrocatalytic activity for diclofenac degradation, 283 (2016) 514-523.
- [57] F. Wu, X. Hu, J. Fan, E. Liu, T. Sun, L. Kang, W. Hou, C. Zhu, H.J.P. Liu, Photocatalytic activity of Ag/TiO₂ nanotube arrays enhanced by surface plasmon resonance and application in hydrogen evolution by water splitting, 8 (2013) 501-508.
- [58] Y. Wang, Z. Li, Y. Tian, W. Zhao, X. Liu, J.J.M.L. Yang, Facile method for fabricating silver-doped TiO₂ nanotube arrays with enhanced photoelectrochemical property, 122 (2014) 248-251.
- [59] S. Sreekantan, S.M. Zaki, C.W. Lai, T.W.J.M.s.i.s.p. Tzu, Copper-incorporated titania nanotubes for effective lead ion removal, 26 (2014) 620-631.
- [60] T. Raguram, K.J.A.P.A.M.S. Rajni, Processing, Synthesis and analysing the structural, optical, morphological, photocatalytic and magnetic properties of TiO₂ and doped (Ni and Cu) TiO₂ nanoparticles by sol-gel technique, 125 (2019).
- [61] Z. Xiong, J. Ma, W.J. Ng, T.D. Waite, X.J.W.r. Zhao, Silver-modified mesoporous TiO₂ photocatalyst for water purification, 45 (2011) 2095-2103.
- [62] D. Lan, M. Qin, R. Yang, S. Chen, H. Wu, Y. Fan, Q. Fu, F.J.J.o.c. Zhang, i. science, Facile synthesis of hierarchical chrysanthemum-like copper cobaltate-copper oxide composites for enhanced microwave absorption performance, 533 (2019) 481-491.
- [63] J. Parker, R.J.A.P.L. Siegel, Calibration of the Raman spectrum to the oxygen stoichiometry of nanophase TiO₂, 57 (1990) 943-945.
- [64] J.C.-S. Wu, C.-H.J.J.o.P. Chen, P.A. Chemistry, A visible-light response vanadium-doped titania nanocatalyst by sol-gel method, 163 (2004) 509-515.

- [65] T. Morikawa, R. Asahi, T. Ohwaki, K. Aoki, Y.J.J.J.o.A.P. Taga, Band-gap narrowing of titanium dioxide by nitrogen doping, 40 (2001) L561.
- [66] A. Mumtaz, N.M. Mohamed, M.I. Irshad, A. Yar, M.S.M.J.i.j.o.h.e. Saheed, Mutual effect of extrinsic defects and electronic carbon traps of M-TiO₂ (M= V, Co, Ni) nanorod arrays on photoexcited charge extraction of CdS for superior photoelectrochemical activity of hydrogen production, 43 (2018) 14388-14405.
- [67] E. Alsharaeh, T. Bora, A. Soliman, F. Ahmed, G. Bharath, M. Ghoniem, K.M. Abu-Salah, J.J.C. Dutta, Sol-gel-assisted microwave-derived synthesis of anatase Ag/TiO₂/GO nanohybrids toward efficient visible light phenol degradation, 7 (2017) 133.
- [68] J. Ananpattarachai, P.J.J.o.E.S. Kajitvichyanukul, P.B. Health, Photocatalytic degradation of p, p'-DDT under UV and visible light using interstitial N-doped TiO₂, 50 (2015) 247-260.
- [69] N. Bao, L. Shen, T. Takata, K.J.C.o.M. Domen, Self-templated synthesis of nanoporous CdS nanostructures for highly efficient photocatalytic hydrogen production under visible light, 20 (2008) 110-117.
- [70] E. Sitara, H. Nasir, A. Mumtaz, M.F. Ehsan, M. Sohail, S. Iram, S.A.B.J.N. Bukhari, Efficient photoelectrochemical water splitting by tailoring MoS₂/CoTe heterojunction in a photoelectrochemical cell, 10 (2020) 2341.
- [71] S. Vinoth, W.-J. Ong, A.J.J.o.c. Pandikumar, i. science, Sulfur-doped graphitic carbon nitride incorporated bismuth oxychloride/Cobalt based type-II heterojunction as a highly stable material for photoelectrochemical water splitting, 591 (2021) 85-95.
- [72] J. Huang, T. Liu, R. Wang, M. Zhang, L. Wang, H. She, Q.J.J.o.c. Wang, i. science, Facile loading of cobalt oxide on bismuth vanadate: proved construction of pn junction for efficient photoelectrochemical water oxidation, 570 (2020) 89-98.
- [73] K.R. Nandanapalli, D. Mudusu, J.-S. Yu, S.J.J.o.c. Lee, i. science, Stable and sustainable photoanodes using zinc oxide and cobalt oxide chemically gradient nanostructures for water-splitting applications, 558 (2020) 9-20.
- [74] H. She, P. Yue, X. Ma, J. Huang, L. Wang, Q.J.A.C.B.E. Wang, Fabrication of BiVO₄ photoanode cocatalyzed with NiCo-layered double hydroxide for enhanced photoactivity of water oxidation, 263 (2020) 118280.
- [75] A. Mumtaz, N.M. Mohamed, M. Mazhar, M.A. Ehsan, M.S.J.A.a.m. Mohamed Saheed, interfaces, Core-shell vanadium modified titania@ β -In₂S₃ hybrid nanorod arrays for superior interface stability and photochemical activity, 8 (2016) 9037-9049.
- [76] S. Chen, M. Malig, M. Tian, A.J.T.J.o.P.C.C. Chen, Electrocatalytic activity of PtAu nanoparticles deposited on TiO₂ nanotubes, 116 (2012) 3298-3304.
- [77] R. O'Hayre, M. Nanu, J. Schoonman, A.J.T.J.o.P.C.C. Goossens, Mott-Schottky and charge-transport analysis of nanoporous titanium dioxide films in air, 111 (2007) 4809-4814.
- [78] L. Heshmatynezhad, F. Jamali-Sheini, A.J.M.R.E. Monshi, Transient photocurrent response of Bi₂S₃/rGO nanocomposites synthesized by UV-assisted sonication method, 6 (2019) 086332.
- [79] D. Chaudhary, S. Singh, V. Vankar, N.J.I.J.o.H.E. Khare, A ternary Ag/TiO₂/CNT photoanode for efficient photoelectrochemical water splitting under visible light irradiation, 42 (2017) 7826-7835.
- [80] J. Ma, X. Tan, T. Yu, X.J.I.J.o.H.E. Li, Fabrication of g-C₃N₄/TiO₂ hierarchical spheres with reactive {001} TiO₂ crystal facets and its visible-light photocatalytic activity, 41 (2016) 3877-3887.